Fusion of ice thickness from passive microwave data and ice ocean model for improved estimation

by

Harveen Janjua

A thesis
presented to the University of Waterloo
in fulfillment of the
thesis requirement for the degree of
Master of Applied Science
in
System Design Engineering

Waterloo, Ontario, Canada, 2015

I hereby declare that I am the sole author of this thesis. This is a true copy of the thesis, including any required final revisions, as accepted by my examiners.

I understand that my thesis may be made electronically available to the public.

Abstract

The ice cover in the perennial region of the Arctic Circle has reduced significantly in recent years. Various models are available to predict the spatial and temporal evolution of the ice cover.Predictions from these models can be improved by incorporating satellite observations by the technique of data assimilation.

In this thesis, ice thickness observations from Advanced Microwave Sensing Radiometer Earth (AMSR-E) and Moderate Resolution Imaging Spectro-Radiometer (MODIS) remote sensors are fused with that from an ice-ocean model using an optimal interpolation technique. It is assumed that the background error covariance matrix is static and the spatial correlations are modelled using a diffusion operator. The observation error covariance matrix is diagonal and the observation operator is saturated to a threshold of 0.2 m for ice thickness observations from AMSR-E because ice thickness is negatively correlated to the polarization ratio for thin ice up to 0.2 m only. It is observed that when more observations are available the analysis from data fusion is closer to ice charts produced by Canadian Ice Services (CIS).

One possible application of the system developed is in areas where ships need to be safely routed through ice infested water. This thesis presents a small example that tries to find the path for a ship through thick ice. The impact of fusing perturbed observations with ice thickness data inferred from a satellite image on the ice thickness traversed and distance travelled is investigated.

Acknowledgements

I would like to thank my supervisor, Prof. Andrea Scott and Prof. Kumaraswamy Ponnambalam, for patient guidance, encouragement and advice that they have provided throughout my time as their student. I have been so lucky to have supervisors who cared so much and responded to my questions and queries promptly. Also, I would like to thank my readers Prof. Alexander Wong and Prof. Nasser Lashgarian Azad for providing constructive feedback and kindly reviewing my thesis.

I must express my gratitude to Vicky, my husband, for his continued support and encouragement. I was continually amazed by his willingness to proof read countless pages of mathematics, and by the patience of my mother, father, brother and in-laws who experienced all the ups and downs of my research.

Completing this work would have been all the more difficult were it not for the support and friendship provided by Apurva Narayana, Dietra Sawh and Mohmmadreza. I am indebted to them for their help.

Dedication

I dedicate my thesis to my father Dr. P. S. Minhas. I would like to express my deepest indebtedness through this dedication.

Table of Contents

List of Tables

List of Figures

List of Symbols

Symbol	Definition
a	normalization factor of C matrix
A	analysis error covariance matrix
B	background error covariance matrix
C	correlation matrix
C_h	horizontal correlation matrix
C_v	vertical correlation matrix
D	diagonal matrix of background error standard deviation
e^b	error in background estimate
e^o	error in the observation
e^a	analysis error
H	observation operator maps state to observation space
H_m	observation operator maps state to observation in analysis box space
i	one step in the zonal direction
j	one step in in the meridional direction
K	Kalman gain
k	time index for Kalman filter
m	the number of observation in new defined domain of square box around each state
n	number of states
nt	one step in time direction
p	number of observations
q	diffusion operator

Q	noise covariance
R	observation error covariance matrix
R_m	observation in analysis box error covariance matrix
Source	heat generation element
t	time
u	x coordinate in the zonal (east - west) direction
v	y coordinate in the meridional (north - south) direction
v_k	random number
W	weight matrix
x^b	background state from the model
x^a	analysis state or optimal state
x^t	true state
y	observations
y_m	observations in analysis box
α	the diffusion coefficient
ϕ(u,v,t)	scalar field function of time and distance
ψ	matrix with ice thickness values

List of Acronyms

Acronym	Definition
3D-VAR	3 dimensional Variational method
AMSR-E	Advanced Microwave Sensing Radiometer Earth
BIO	Bedford Institute of Oceanography
BLUE	Best Linear Unbiased Estimator
CIOM	Community Ice Ocean Model
CIS	Canadian Ice Services
CRREL	U.S. Army Cold Regions Research and Engineering Laboratory
EnKF	Ensemble Kalman Filter
ESMR	Electrically Scanning Microwave Radiometer
GEM	Global Environmental Multiscale
GPS	Global Positioning System
JAXA	Japan Aerospace Exploration Agency
MANICE	Manual of Standard Procedures for Observing and Reporting Ice Conditions
MODIS	Moderate Resolution Imaging Spectro-Radiometer
NASA	National Aeronautics and Space Administration
NSR	Northern Sea Route
NWP	Northwest Passage
NWP	Numerical Weather Prediction
OI	Optimal Interpolation
PDE	Partial Differential Equation
RTM	Radiative Transfer Model

SAR	Synthetic Aperture Radar
SCM	Successive Correction Method
SMMR	Scanning Multichannel Microwave Radiometer
SSM/I	Special Sensor Microwave/Imager
TBs	Brightness Temperatures
VIS/IR	Visible Infrared
WMO	World Meteorological Organization

Chapter 1

Introduction

The melting ice in the Arctic is a matter of major concern. The Arctic region is extensively monitored by satellites that detect the extent of ice coverage [3]. Existing historical data mainly documents the diminishing ice extent rather than ice thickness. This is due to constraints in measuring ice thickness from remotely sensed data.

The sea ice cover distribution monitored in the Arctic basin during the periods of 1958-1970 and 1993-1997 has indicated that the average sea ice thickness in the area covered by open water and first year ice increased from 0.19 m to 0.30 m which was balanced by an 11% reduction in level-multiyear ice (i.e. ice accumulated over 2 or more years)[4]. A later study by NASA [5] has revealed that the thickest and the oldest ice is melting at a faster rate than the younger and the thinner ice. The multiyear ice is diminishing at a rate of 15.1% per decade. As a result, the ice cover in the perennial region of the Arctic Circle was reduced by 55% by 2012 when compared with that in 1980 [5].

Melting ice in the Arctic region has facilitated ships to route their path through this region. The advantage is the shorter route and the reduced travel time over the southern

routes. But sometimes ships become stuck in the thick ice cover, thus making it difficult to travel. Therefore, information on the spatial distribution of ice thickness along their route should help navigation through the Arctic region. Such information would further help in untroubled movement of local people residing in the Arctic and for transporting goods and materials. Moreover, the thick ice can even hinder the working of icebreaker ships.

Data assimilation is a technique in which output from a model and observations are combined to produce a better estimate of the state. This is done in two cycles i.e. prediction and correction. In the prediction cycle, estimates of the current state variables are produced using prognostic model. These states have certain uncertainties associated to them. In the correction cycle, the state estimate is updated using weighted averages between background and observations with more weight being given to estimates with higher certainty [6]. The estimates produced are then fed to the model to have a new initial condition. It has been shown that coupled ice-ocean models sometimes overestimate the thickness of the thin ice while underestimating that of the thick ice [7] [8]. Hence, there seems a need to modify the estimated sea ice thickness by combining the model state with the satellite observations for improving the estimates of ice thickness states.

In this thesis, ice thickness from an ice-ocean coupled model is fused with the satellite observations to produce better estimates of the ice thickness states. Data assimilation equations are used to combine observations with a model state, but there is no feedback to the model. This way of combining the ice estimates and the observations is data fusion.

Many methods have been used with different remote sensors to estimate sea ice thickness [9] [10] [11] [12]. In this thesis, results with Advanced Microwave Sensing Radiometer Earth (AMSR-E) and Moderate Resolution Imaging Spectro-Radiometer (MODIS) observations are fused with ice thickness from the model for the month of January 2007. AMSR-E is a passive microwave radiometer and MODIS is a visible/infrared sensor. Each of

these sensors has different mechanism of measuring the ice thickness, for example, AMSR-E measures the brightness temperature while MODIS uses the surface temperature to estimate ice thickness.

Several techniques are available for data assimilation such as Kalman filter, optimal interpolation, 3D-VAR and 4D-VAR. All these methods use observations and state estimates with noise and other inaccuracies to produce better estimates of the state In this thesis, the Kalman filter could not be used because of its inefficiency to give optimal results for large domain sizes and also there is no prognostic model available to propagate the state and the error covariance matrix forward in time. Alternatively, optimal interpolation is used, which applies Best Linear Unbiased Estimator (BLUE) over a small area of the study with fewer observations in its vicinity.

For validation, the daily ice charts prepared by the Canadian Ice Service (CIS) were analysed to produce a map with regions classified as new, young, thin, medium or thick ice. The chart data was then compared with results from data fusion to verify its validity and draw conclusions as to its deviation from an independent state of ice thickness.

This thesis also presents on the calculation of various parameters for data assimilation technique. The background error covariance matrix is calculated by solving the diffusion equation at each point in the background. It is applied with Dirichlet boundary condition on the sea coast and Neumann boundary condition on the open ocean boundary. The observation operator is calculated by applying linear forward model to ice thickness values below a threshold and a saturation function to ice thickness values above threshold. AMSR-E and MODIS ice thickness observations have a threshold of 0.2 m and 0.5 m respectively. Various experiments were done to evaluate values for AMSR-E and MODIS observation error standard deviation.

Applications of data assimilation have markedly increased in recent years, especially in geosciences, weather forecasting and hydrology [13], in addition to GPS navigation systems [14] and pollution source estimation. One of the aims of using data fusion technique in this thesis is to compute ice thickness estimates to find optimal routes for ships and hence help in their safer navigation. It is believed that if ships know the ice thickness at various points along their route, then they can travel with shorter and reduced time consuming routes and avoid any disturbances that can be caused by thick ice hindering their route. Data fusion was used to predict ice thickness for areas through which ships must travel. This information was used to provide the path through the ice and can result in better navigation.

The outline of the thesis is as follows - Chapter 2 presents background and a literature review divided into four sections, namely, remote sensing observation, data assimilation, data assimilation for sea ice thickness and ships routing through the Canadian Arctic. Chapter 3, presents description of various inputs to the model. These inputs include ice thickness data from Community Ice Ocean Model (CIOM) of CIS, remote sensors AMSR-E and MODIS and daily sea ice charts to validate our results. Chapter 4 describes the general idea of data assimilation and reviews the Kalman filter and the optimal interpolation.

Chapter 5, presents results for ice thickness estimation under various sections. The first section describes the calculation of the background error covariance matrix, observation operator and observation error covariance matrix. The second section is for improving estimates for sea ice thickness through various experiments. The first experiment involves analysing changes in observation error standard deviation for MODIS and AMSR-E, followed by analysing estimates with and without saturation of the observation operator for AMSR-E and MODIS and then comparing ice thickness estimation results when AMSR-E observations are fused to model states, for January 2007, with ice charts. This section

ends by demonstrating a simple but realistic example which tries to improve ship paths by estimating ice thickness values. Chapter 6, presents the conclusion of the research work.

Chapter 2

Background and Literature Review

This chapter presents a review of remote sensing, data assimilation and ship routing. It discusses remote sensors used to measure sea ice extent. It then presents studies of sea ice extent of the Arctic region for the period 1958-1970 and 1993-1997. The chapter then continues with the evolution of data assimilation methods. Towards the end of the chapter, data assimilation is discussed in the context of sea ice concentration and sea ice thickness simulation. The chapter closes with a discussion on improving navigational routes for ships to traverse through the Canadian Arctic.

2.1 Remote sensing observation of sea ice

The percentage of sea ice cover in a given area of the ocean is defined as sea ice concentration. This information is useful to navigators and weather forecasters. Direct records of ice concentration were kept in 1950 but gained momentum in the 1970's due to the use of satellite borne remote sensors. Measurements began in 1972 with the electrically

scanning microwave radiometer (ESMR) instrument, followed by NASAs scanning multichannel microwave radiometer (SMMR) satellite and continued with the special sensor microwave/imager (SSM/I) and the advanced microwave scanning radiometer - earth (AMSR-E). Each of these instruments had their own mechanism to measure the ice parameters. The ESMR instrument only senses horizontally polarized radiation, while SMMR, SSM/I and AMSR measures both horizontally and vertically polarized sensors. All of these sensors measure brightness temperature [15]. These are passive remote sensors which detect energy emitted by the earth using naturally occurring energy from the sun. They can measure energy reflected at night only if the amount of energy is large enough to be recorded [16]. Passive microwave sensors are different from active sensors, which emit radiation towards the target and then measure reflected energy. A good example of an active sensor is synthetic aperture radar (SAR).

The sea ice extent was studied by remote sensors for the period 1993 —1997 and 1958 —1970. The fractional extent of first year ice increased from less than 20% of the Arctic area in 1958 –1970 to almost 33% of it in 1993 –1997. While the coverage of 1 –2 m ice increased from 24% to 33%, there was a decrease in all thicker ice categories. The overall volume loss was about 32% [4], which is 8% less than the value reported by Rothrock [17]. The latest climate model predictions also indicate that the September ice extent will drop to 1.7 million km square in the mid 2040's and reach an ice-free state in 2054 –2058, considering that there is a high emission state of carbon dioxide and methane [18]. In such a rapidly changing ice cover over the Arctic, shipping routes are expected to be open in the near future and the Arctic maritime activities will become more frequent [19] [20].

2.2 Data assimilation

Data assimilation is defined as a process in which observations are combined with the information provided by a prognostic model to produce a better estimate of the state. This improved estimate is then used to initialize the next model forecast.

The need for data assimilation arose when large quantities of meteorological and oceanography data became available. This data included for example —air pressure, temperature, ocean currents, waves and ice thickness. The first step to numerical estimation was objective analysis [21]. The analysis was manually prepared and represented in the form of charts or contour maps. Later, these manual graphic interpolations were replaced by mathematical models, such as 2D polynomial interpolation [22]. This step was largely motivated, due to improved knowledge of atmospheric dynamics and was used to produce better numerical weather forecasts [23][21] [24].

The main idea underlying objective analysis was the statistical estimation [25] [26] [27], where observations have a spatial covariance which was predetermined and stationary. This idea was too complicated and computationally expensive. Thus, other methods like the successive correction method (SCM) [28] were implemented in weather forecasts [21].

Gilchrist and Cressman [29] used polynomial interpolation to fit a second degree polynomial to observations in a rectangular grid surrounding each point in the background state. The interpolation could not provide enough data for the model as in numerical weather prediction (NWP) there were 10^7 background states and 10^4 observations [21]. This insufficiency of data required a first guess estimate of the atmosphere to generate initial conditions for the forecast [30]. The first guess of the background state should be the best estimate of the atmosphere. Short forecasts with first guess [26] [30] improved the whole process [21].

Statistical combination of observations and short range forecasts played a very important role in data assimilation as they brought in the concept of combining dynamics and statistical data. Many data assimilation techniques have been developed that differ in their cost, optimality and usability [31]. These techniques can be discussed from many angles depending on the background and preferences (control theory [32] [33], estimation theory [34], probability theory [34] [35] [36] and variational analysis [37] [31]).

Recent methods include the Kalman filter [38], ensemble Kalman filter [39], optimal interpolation [26], 3D-VAR [40] [41] and 4D-VAR.

2.3 Data assimilation for sea ice

Data assimilation of sea ice observations has been carried out for the past 20 years. It started with the application of Kalman smoothing, by Thomas and Rothrock in 1989 [42] [43], to assimilate sea-ice concentration data with multichannel satellite passive microwave data. They combined sea ice concentration from a model with sea ice concentration observations from the satellite. This work was then extended by Thomas [44] by doing additional sea-ice thickness computation. They used observed sea-ice motions, winds and concentration plus a thermodynamic sea-ice model to produce spatially varying Arctic sea-ice thickness distributions.

In 2003, Lisaeter [45] presented data assimilation of passive microwave sea-ice concentration with an Ensemble Kalman Filter (EnKF). They concluded that the assimilation of ice concentration data is a possible way of simulating the ice cover, but it will not correct the underestimated model ice thickness.

In 2004, Lieser [46] assimilated SSM/I satellite derived sea-ice concentration data with

a stand-alone sea-ice model using an optimal interpolation (OI) technique. The aim was to optimize sea-ice conditions for a short term sea-ice forecast of 5-10 days, assuming that the ice thickness is constant and the volume and concentration vary in direct proportion to each other. It was observed that this combination of technique and assumption improved the sea ice concentration estimate by 10%, but no improvement in ice thickness was observed.

In 2000, Meier [47] was the first to attempt to assimilate ice motion data into a large-scale model of the Arctic sea ice cover. OI was used to assimilate sea ice velocity. This increased the accuracy of the model but the assimilation indicates unrealistic changes of the sea-ice thickness in some regions of the Arctic.

Later, in 2002, Arbetter [48] assimilated SSM/I satellite-derived data with modelled ice velocities in a large-scale Arctic sea ice model. It was observed that for both years 1990 and 1998, the computed ice extent was in agreement with the observed estimates but excessive ice melt was observed in the central region.

In 2003, Meier and Maslanik [49] showed that using OI scheme improves ice thickness estimation in both the coastal and the non-coastal regions. It is also believed that if proper weights are given to local conditions like the proximity to the coast, the ice thickness and the wind forcing, this will further reduce the error and give better estimates.

Zhang, in 2003, [50] assimilated passive microwave sea-ice motion data into a sea-ice ocean model using an OI scheme. Ice draft from assimilation was observed to be closer to submarine draft measurements. Lindsay [51] extended this work for a ten month period, and Lindsay and Zhang [52] extended the work of Zhang [50] by incorporating into their model a nudging scheme using a non-linear weighting function to assimilate passive microwave sea-ice concentration data.

Duliere and Fichefet [53] did many experiments on the assimilated sea-ice concentration

and velocity, and developed a model of the Arctic sea-ice pack to improve sea ice thickness estimation. They utilized an OI scheme. The results indicate that under certain conditions, depending on assimilation weights and type of the model error, the sea-ice velocity assimilation improves the model performance.

Stark [54] assimilated SSM/I ice concentration using an OI method. Wang [55] combined OI and a nudging scheme to assimilate ice concentration. In these studies it was observed that assimilation of observed ice concentration in the ice ocean models improved the ice concentration estimates, but the improvement in ice thickness was very small. In a recent study, Tietsche [56] assimilated the ice concentration observations into a climate model and updated the sea ice thickness using a proportional dependence between the concentration and the mean thickness. They assumed implicit correlation between the ice thickness and the concentration [20].

The studies mentioned above indicate that data assimilation improves the model estimate of the assimilated variable(s) i.e. sea ice thickness and sea ice concentration. Hence, data assimilation can be applied to improve the sea ice model short-term sea-ice forecasts.

2.4 Ship routing through Canadian Arctic

In the last few years there has been an increase in the energy consumption and the price of oil. To access the natural resources in the Arctic region new shipping routes are being considered. Accelerated Arctic ice melting has resulted in improved human access to the Arctic area. In 2008, the Northern Sea Route (NSR) along Russia and the Northwest Passage (NWP) through Canadian Arctic archipelago were open to allow fast navigation between the Pacific and the Atlantic oceans [57].

It has been observed that NSR and NWP are shorter routes and thus are less expensive when compared to routes passing through the southern Suez Canal and Panama Canal. The Arctic region generally has a harsh environment year-round, which cause difficulties to ships carrying natural resources or goods. It is very hard to simulate navigation routes through this region, but on the other hand it is very beneficial due to the presence of natural resources.

To compute the navigational route, it is necessary to have a transit model, which describes every piece of information required for navigation. La Prairie [58] suggested a model to estimate the cost of transit by considering the relationship between the thrust of a ship and ice resistance. This was followed by models from Patey and Riska [59], Kamesaki [60], which numerically analysed and determined the optimal route by estimating the distance, speed and ice breaker fees. On the other hand, CRREL (U.S. Army Cold Regions Research and Engineering Laboratory) developed a NSR transit model [61]. They used a probabilistic distribution for the ice model and Monte Carlo iteration to find navigation routes. CRREL model was later modified by Choi [62] and Ha [63] to include realistic data.

The advantage of the above listed models is that sea ice state along NSR and NWP predicted by models is useful towards finding the optimal path through the thick ice. Real time update of ice and environment data from satellites is the required input for these models.

2.5 Summary

The data from passive sensors indicated that there is substantial decrease in ice cover over the Arctic. This has facilitated ships to route through NSR and NWP for shorter

distance and reduced travel time. This chapter describe studies on the application of data assimilation with various remote sensor satellites data to estimate ice concentration, ice thickness and ice velocity for short term forecast or large scale data. At end of this chapter transit models are discussed, which estimate the cost of a ship travelling through ice-infested water. The next chapter describes various inputs to data assimilation technique, such as ice thickness values from the ice ocean model, AMSR-E and MODIS sensors, and the ice charts.

Chapter 3

Data

This chapter presents the various data sets used for the research, which consists of output from a coupled sea ice ocean model, data from the AMSR-E sensor and the MODIS sensor, and ice chart data. The sea ice ocean model solves equations to estimate the ice-ocean state on the east coast of Canada. AMSR-E and MODIS are both remote sensing instruments, which measure brightness temperature and surface temperature respectively to estimate sea ice thickness. Lastly, in this chapter, ice charts are discussed. These ice charts are used to assess results from data fusion.

3.1 Ice ocean model

The ice ocean model is the Community Ice Ocean Model (CIOM), described by Yao [64] that covers the east coast of Canada. It was originally developed by the Bedford Institute of Oceanography (BIO), Canada's largest centre for the ocean research. Then BIO and CIS collaborated to further develop this model [16].

The ice ocean model has 24 ice thickness categories plus one category for the open water fraction. The input to the CIOM model is atmospheric forcing data from the Canadian Global Environmental Multiscale (GEM) model [65]. This data is available for short term regional forecasts and is refreshed every 3 hours [66]. The ice model describes various aspects of the ice state. Some of the important elements include concentration, thickness, speed, direction and location [16].

The spatial resolution of the model is 0.45˚in latitude and 0.6˚in longitude. In this model three-dimensional equations for ocean velocity, temperature, salinity and thickness distribution are solved. The sea ice model equations describe both ice dynamics and thermodynamics [66].

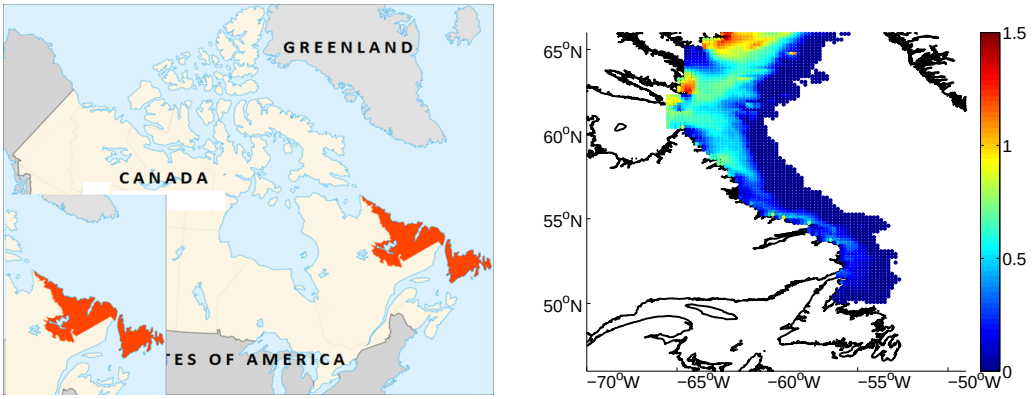

(a) East Coast of Canada, Labrador Coast

(b) Discretized Labrador Coast with ice thickness

Figure 3.1: Region of study shown in political map in panel (a) and as descritized form with color map representing ice thickness in panel (b)

Figure 3.1a, shows a map of Canada with the study region, which is the east coast of Canada around the Labrador Coast, shown in the insets, and figure 3.1b shows the same

region in discretized form. The ice thickness shown in figure 3.1b needs to be represented in a vector form. It is reordered to form the column vector $\mathbf{x}^b$, where each element of the column represents the ice thickness at a given latitude and longitude.

3.2 Advanced Microwave Sensing Radiometer Earth (AMSR-E) Data

The Advanced Microwave Sensing Radiometer Earth was developed by the Japan Aerospace Exploration Agency with cooperation of U.S. and Japanese scientists. AMSR-E is a twelve channel, six frequency, passive microwave radiometer system. It measures electromagnetic radiation at 6 frequencies (6.9 GHz, 10.9 GHz, 18.9 GHz, 24.5 GHz, 36.5 GHz and 89 GHz). The footprints associated with these frequencies are elliptical with size ranging from 74 km X 43 km for the 6.9 GHz channel to 6 km X 4 km for the 89 GHz channel [15].

Data in higher frequencies on the AMSR-E instrument may be contaminated because the presence of water vapour, rain or clouds can generate spectral signatures similar to those from the sea-ice. Pixels contaminated by the above mentioned atmospheric effects need to be masked out. In previous studies this was done by developing a relationship between the polarization ratio at 36.5 GHz and at a higher frequency of 89 GHz [67] [68]. For the AMSR-E observations used in this thesis, atmospheric contaminated pixels were identified using a radiative transfer model (RTM).

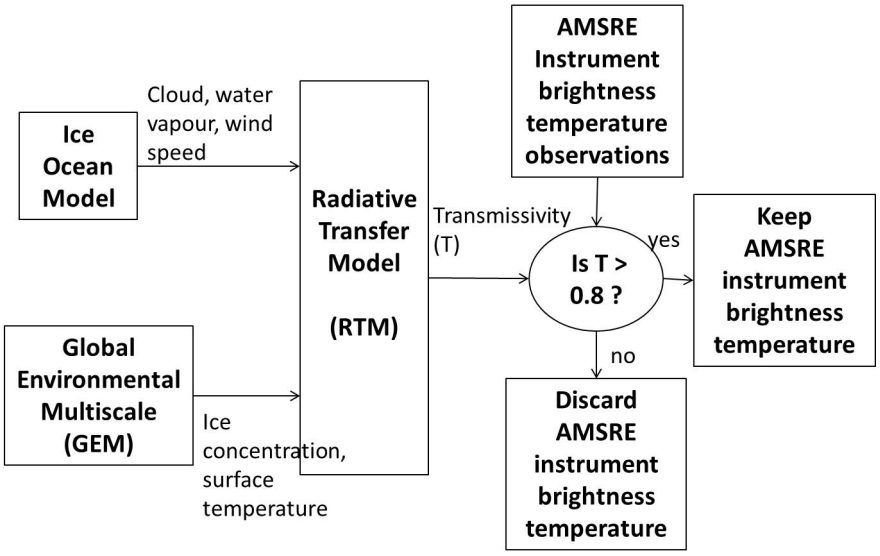

Figure 3.2: Block diagram shows the method used to remove AMSR-E pixels with atmospheric contamination

The block diagram shown in figure 3.2 gives a better understanding of the processing of AMSR-E data. It mainly consists of four blocks: Ice-Ocean Model, Environment Canada's Global Environmental Multiscale (GEM), Radiative Transfer Model (RTM) and AMSR-E instrument brightness temperature observations.

The output from GEM has a spatial resolution of 0.45°in latitude and 0.6°in longitude with data available every 3 hours. This output is bi-linearly interpolated in space and linearly interpolated in time to the AMSR-E observations location and time [2].

The RTM was developed by Wentz and Meissner [69]. It is used to calculate the atmospheric transmissivity (T), or atmospheric influence. The model assumes that atmospheric transmissivity is a function of the surface temperature through the absorption coefficient for the cloud liquid water [2]. A transmissivity value of 1.0 indicates clear atmosphere and

0 indicates opaque atmosphere. The present study uses the RTM to select only pixels with transmissivity greater than 0.8.

The polarization ratio is used to calculate ice thickness from brightness temperature, at location where the transmissivity is more than 0.8. The polarization ratio is defined as the ratio of the difference between the vertically and the horizontally polarized brightness temperature to the sum of the vertically and the horizontally polarized brightness temperature. A study by Ohshima [9] shows that polarization ratio is negatively correlated to sea ice thickness for thin ice, which is under 0.2 m approximately. In addition, the polarization ratio is not sensitive to sea ice thickness when the ice is more than 0.2 m thick.

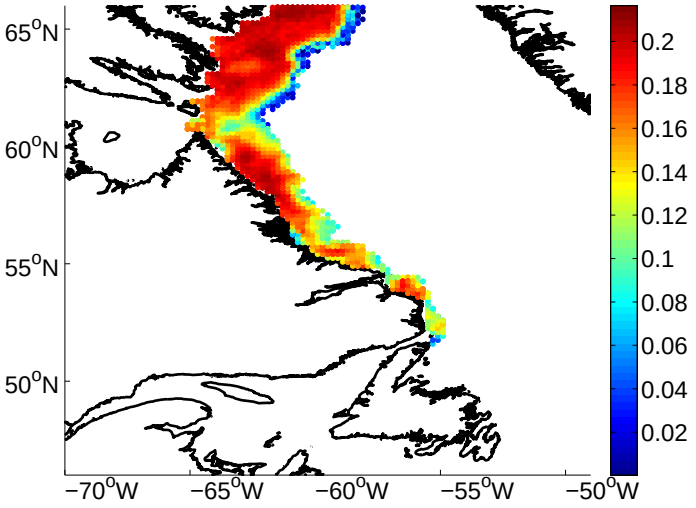

Figure 3.3: Ice thickness observations from AMSR-E polarization ratio with 10.9 GHz frequency channel for January 24, 2007

Ice thickness values for the month of January 2007 are used in the data fusion. Figure 3.3 shows the AMSR-E ice thickness data for January 24, 2007. AMSR-E cannot measure ice of thickness more than 0.2 m. Hence, in figure 3.3 a large region of ice thickness shows up being 0.2 m, indicating the measurement from the sensor is saturated. In this thesis only ice thickness calculated using the 10.9 GHz channel from AMSR-E.

3.3 Moderate Resolution Imaging Spectro Radiometer (MODIS) Data

The Moderate Resolution Imaging Spectro-radiometer is an instrument on two satellites (Terra and Aqua) flying in NASAs Earth observing system. In 1999, the Terra satellite was launched in an orbit from south to north with a morning (1030 hrs LMT) equatorial crossing. In 2002, the Aqua satellite was launched in an orbit from north to south with an afternoon (1330 hrs LMT) equatorial crossing. These two satellites with different orbits allow us to image the same area at different times of the day. Also they cover the entire earth in one or two days. MODIS instruments on-board Terra and Aqua satellites, capture data in 36 spectral bands ranging in wavelength from 0.4 μ to 14.4 μ and at varying spatial resolutions (2 bands at 250 m, 5 bands at 500 m and 29 bands at 1 km) [70]. Computation

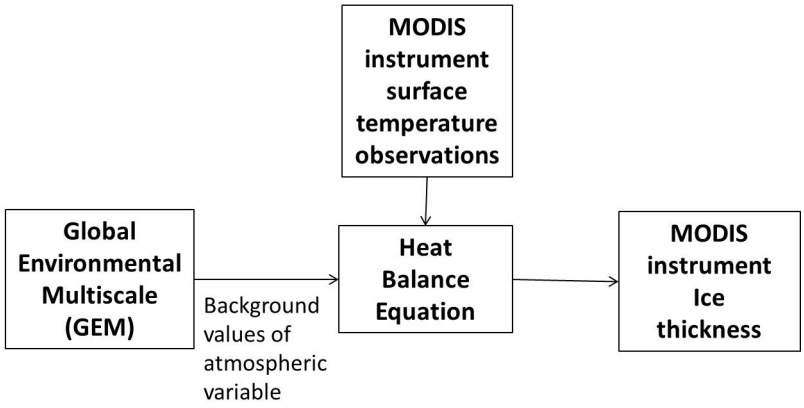

Figure 3.4: Block diagram shows MODIS ice thickness calculation from heat balance equation

of ice thickness from MODIS instrument consists of three blocks (Figure 3.4). These blocks are GEM, heat balance equation and MODIS instrument surface temperature observations.

It is difficult to measure surface temperature from the source when cloud cover is present. The MODIS products used have cloud masks built to prevent clouds from being interpreted as ice and snow. It uses the MOD29 product, prepared by the National Snow and Ice data centre. These products are generated using the MODIS sensor radiance data products (MOD021KM and MYD021KM), the geolocation products (MOD03 and MYD03), and the cloud mask products (MOD35_L2 and MYD35_L2) [70]. Another limitation of MODIS is that during the day time it is difficult to estimate surface temperature due to uncertainty associated with the surface reflection and the shortwave radiation, which are parameters in the daytime heat balance equation. Hence, night time observations from midnight to dawn are used. Observations from Aqua platform sensors are used because nighttime observations are only available from Aqua and also this platform carries the AMSR-E sensor hence making it easy to compare MODIS and AMSR-E [2].

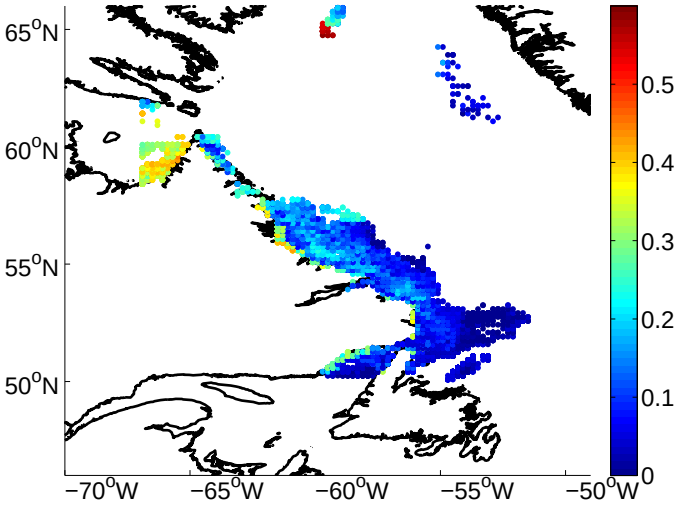

Figure 3.5: Ice thickness observations from MODIS sensor for January 24, 2007

The ice thickness is calculated from a heat balance equation at the interface between the ice or snow and the atmosphere, described in detail in [11] [12] [71]. The input to heat balance equation is the surface temperature from MODIS and atmospheric fields - wind speed, cloud fraction and surface pressure from the GEM model. These atmospheric fields have a different resolution so they need to be interpolated linearly to observation time and bilinearly to observation locations. [2].

Other limitations of using surface temperature from MODIS to calculate ice thickness

arise due to the heat balance approach, as it is sensitive to assumptions regarding snow covering the ice. It typically assumes a linear temperature profile through the ice and snow, which limits its range of applicability to ice less than approximately 0.5 m in thickness.

In this thesis, ice thickness values for the month of January 2007 over the east coast of Canada are used. An example of ice thickness calculated using the heat balance equation is shown in Figure 3.5 for January 24, 2007. MODIS data cannot be used reliably to measure ice thickness of more than 0.5 m. Hence, in figure 3.5 all values of ice thickness more than 0.5 m are masked.

3.4 Ice charts data

The results obtained from data fusion need to be compared against independent data to assess the quality of assimilation. The observations used for this purpose are the daily ice charts prepared in near-real time by CIS [72]. CIS produces daily ice analyses for all the Canadian ice-infested waters. Many users rely on these ice analyses for planning safe and efficient marine navigation activities.

Ice analyses are produced manually by analysts who combine the information from satellite imagery, ship and aircraft reports and also the analyses from the previous day. The satellite imagery used comes from SAR to a large extent and hence the ice charts are considered independent from AMSR-E and MODIS data. This analysis done by ice analysts is labour intensive and should be completed in a required time frame. For this reason, analysts mostly focus on high priority areas such as those with ongoing shipping and ice breaking activity. It is very difficult to maintain consistency throughout the domain [2].

Table 3.1: Stages of ice development based on ice thickness [1]

Ice thickness	Stage of development
less than 10 cm	New Ice
10 - 30 cm	Young Ice
30 - 70 cm	Thin First Year Ice
70 - 120 cm	Medium First Year Ice
more than 120 cm	Thick First Year Ice

Ice charts are available on the CIS website both for the concentration and the stages of development of the ice according to World Meteorological Organization (WMO) standards [1]. The stages of development are related to the thickness as shown in table 3.1. New ice refers to the ice that is less than 10 cm thick. It includes fine plates of ice suspended in water. The elastic crust of thin ice can bend due to waves and the ice can easily break into pieces. Young ice is the transition stage between the new and the first year ice. It is less elastic than the new ice but still breaks due to waves. The first year ice is thin ice growth from one year's winter. It is divided into categories: thin, medium and thick based on thickness. Sea ice that has survived at least one summer melt is referred as second-year ice and one that has survived at least two summer seasons is called multi-year ice. Ice thickness data is presented in the charts in the form of an egg code and the details of such codes are provided in MANICE (Manual of Standard Procedures for Observing and Reporting Ice Conditions) [1]. MANICE is an authoritative document for observing all forms of sea, lake and river ice. It describes standard procedures of CIS for observing, recording and reporting ice conditions. Figure 3.6 shows the ice chart for a portion of the

Labrador coast for 24 January, 2007.

When comparing ice chart data with other sources of data, several factors should be taken into account. Firstly, ice analysts prepare ice charts manually and interpretation of data by different analysts can lead to different values. Secondly, there can be errors while converting continuous data images to discrete ice thickness categories. For example, small scale details such as cracks in the ice cover are lost in the preparation of ice charts. Finally, ice charts do not capture the details of ridging, developed by pressure exerted by ice at different stages of ice development [2].

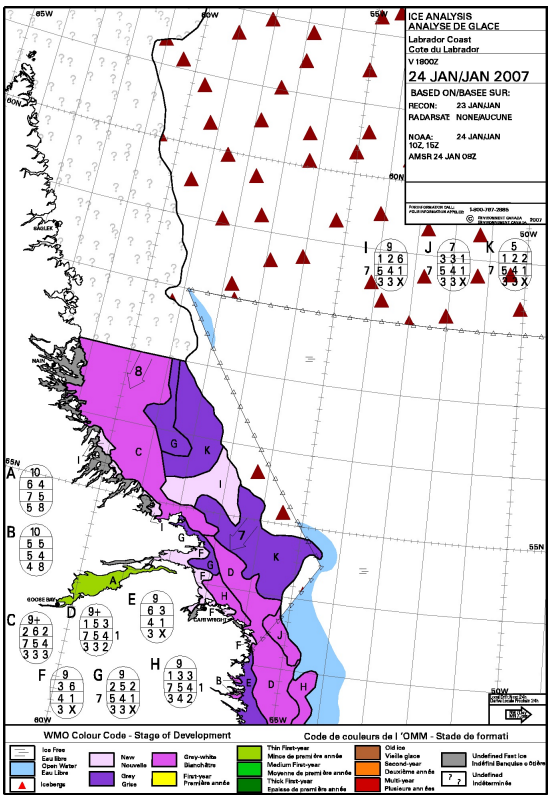

Figure 3.6: Ice chart for January 24, 2007 indicating ice types [1]

3.5 Summary

In this chapter, a brief overview of various inputs to the data fusion technique is provided. These inputs are ice thickness values from ice-ocean model, AMSR-E, MODIS and ice charts. Ice ocean model calculates ice thickness based on solving thermodynamic and dynamic equations. Remote sensors, AMSR-E and MODIS, use brightness temperature and surface temperature respectively to measure ice thickness, while ice charts are manually prepared by analyst by considering predictions for previous day, observational data and remote sensing data, and rely heavily on SAR images. The next chapter explains data assimilation and its methods.

Chapter 4

Data Assimilation and Methodology

Data assimilation is a process in which model output and observations are combined to produce a more accurate state estimate. This state estimate is then used to initialize a model forecast .

Why is data assimilation needed? Why not just use observations for the analysis as the observations represent a measurement of current reality? One problem is that observations do not provide a complete description of the state at every location. Also, sometimes it is required to use current values to predict the future. For example, ice thickness values for tomorrow are based on the observations and model output today. Hence, the observations can be used to constrain prognostic models [13].

The process of data assimilation starts with an initial guess as shown in figure 4.1. The initial condition is given to the model to produce the initial output state. For example, to predict ice thickness for today, the initial condition for today may be yesterday's predicted ice thickness values. Then the assimilation algorithm will combine both the initial condition and observations of today to give the optimal ice thickness values for today. These optimal

values are used as the initial condition for the model to produce the next output state. The output is again combined with observations of the following day to give another optimal set of values that can be used to initialize the model once again. This is the process of data assimilation. The output from assimilation is the best estimate of the current state of the system subject to the optimality condition and all assumptions used to derive the assimilation algorithm. In this thesis a prognostic model is not used to advance the analysis forward in time. Instead states from previous model run are combined with observations each day independently and this process is referred to as data fusion.

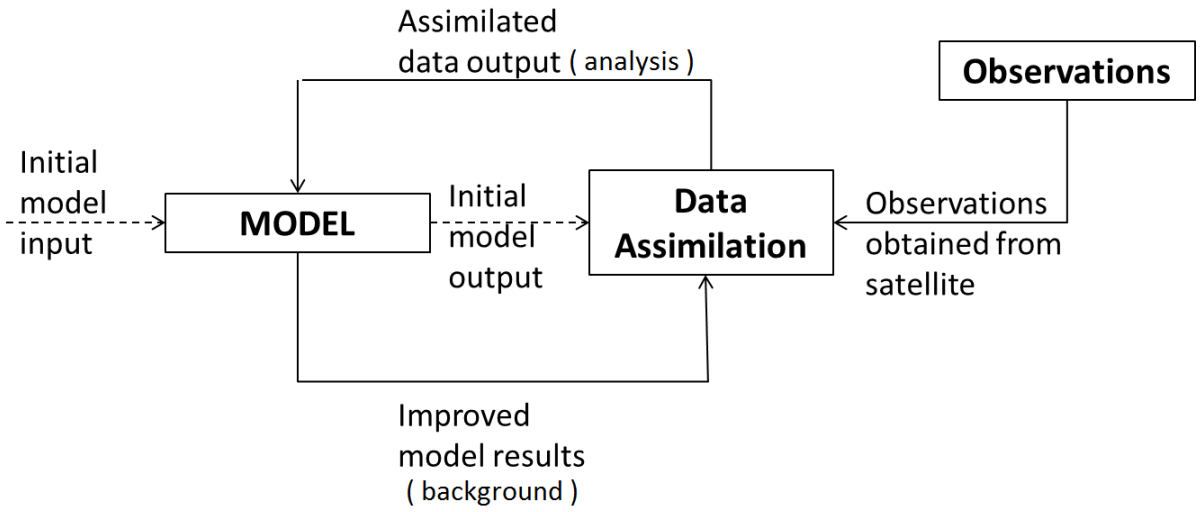

Figure 4.1: Data assimilation block diagram in which model output and observations are combined to provide assimilated data feedback to model

A relevant question is how should different data sources i.e. model output and observations be combined? Clearly, if one is more accurate than the other, then the more accurate one should be given more weight [13]. This concept forms the basis of many data assimilation techniques such as Kalman filter, optimal interpolation (OI), variational techniques.

Each of these techniques differs in their optimality and usage.

4.1 Notation

Consider an n-dimension state vector $\mathbf{x}$ (superscripted with t, b and a to represent true, background and analysis state respectively) and p-dimension observations $\mathbf{y}$. Variables and operators used at various steps of assimilation technique are denoted as

- $\mathbf{x}^{\mathrm{b}}$ - background state from the model, (n)
- $\mathbf{x}^{\mathrm{a}}$ - analysis state or optimal state, (n)
- $\mathbf{x}^{\mathrm{t}}$ - true state, (n)
- $\mathbf{y}$ - observations, (p)
- $\mathbf{e}^{o}$ - observation error ($\mathbf{y}$ - H($\mathbf{x}^{\mathrm{t}}$),(p)
- $\mathbf{e}^{b}$ - background error ($\mathbf{x}^{\mathrm{b}}$ - $\mathbf{x}^{\mathrm{t}}$),(n)
- $\mathbf{e}^{a}$ - analysis error ($\mathbf{x}^{\mathrm{a}}$ - $\mathbf{x}^{\mathrm{t}}$),(n)
- H - observation operator maps state to observation space, (p times n)
- $\mathbf{B}$ - background error covariance matrix $<(\mathbf{x}^{\mathrm{b}} - \mathbf{x}^{\mathrm{t}})(\mathbf{x}^{\mathrm{b}} - \mathbf{x}^{\mathrm{t}})^{T}>$, (n times n)
- $\mathbf{R}$ - observation error covariance matrix $<(\mathbf{y} - \mathrm{H}(\mathbf{x}^{\mathrm{t}}))(\mathbf{y} - \mathrm{H}(\mathbf{x}^{\mathrm{t}}))^{T}>$, (n times n)
- $\mathbf{A}$ - analysis error covariance matrix $<(\mathbf{x}^{\mathrm{a}} - \mathbf{x}^{\mathrm{t}})(\mathbf{x}^{\mathrm{a}} - \mathbf{x}^{\mathrm{t}})^{T}>$, (n times n)

The background state is defined as

$$\mathbf{x}^b = \mathbf{x}^t + \mathbf{e}^b \tag{4.1}$$

where $\mathbf{e}^b$ is the error in background state. The background errors are assumed to have a mean of zero, i.e. $< \mathbf{e}^b >= 0$ (here angled bracket <> represents expectation operator) and background error covariance matrix is $\mathbf{B} =< \mathbf{e}^b(\mathbf{e}^b)^T > = <(\mathbf{x}^{\mathrm{b}} - \mathbf{x}^{\mathrm{t}})(\mathbf{x}^{\mathrm{b}} - \mathbf{x}^{\mathrm{t}})^T >$. The **B** matrix can be static meaning that it does not evolve with the state or can be state dependent. For the present study it is assumed to be static.

Consider a p-dimensional observation vector denoted as **y**, with a given perfect and possibly non-linear observation operator H, which maps state space to observation space. The observations are given by

$$\mathbf{y} = H(\mathbf{x}^t) + \mathbf{e}^o \tag{4.2}$$

where $\mathbf{e}^o$ is the error in the observation. The observation errors are assumed to have mean zero i.e. $< \mathbf{e}^o >= 0$, and error covariance matrix $\mathbf{R} =< \mathbf{e}^o\mathbf{e}^{oT} > = <(\mathbf{y} - \mathrm{H}(\mathbf{x}^{\mathrm{t}}))(\mathbf{y} - \mathrm{H}(\mathbf{x}^{\mathrm{t}}))^T >$. It is further assumed that the background and observation errors are not correlated to each other $< \mathbf{e}^b\mathbf{e}^{oT} >=< \mathbf{e}^o\mathbf{e}^{bT} >= 0$.

The analysis estimate $\mathbf{x}^a$, is defined by

$$\mathbf{x}^a = \mathbf{x}^t + \mathbf{e}^a \tag{4.3}$$

where $\mathbf{e}^a$ is the analysis error matrix. The analysis errors are assumed to have mean zero i.e. $< \mathbf{e}^a >= 0$, and the analysis error covariance matrix is $\mathbf{A} =< \mathbf{e}^a\mathbf{e}^{aT} > = <\mathbf{(x^a - x^t)(x^a - x^t)}^T >$.

4.2 Best Linear Unbiased Estimate

The Best Linear Unbiased Estimate provides the best estimate of the analysis state which is assumed to be a linear combination of the background state $\mathbf{x}^{\mathrm{b}}$ and the observation $\mathbf{y}$, as given in Equation 4.4, assuming unbiased errors . Here $\mathbf{K}$ and $\mathbf{W}$ are weight matrices.

$$\mathbf{x}^a = \mathbf{W}\mathbf{x}^b + \mathbf{K}\mathbf{y} \tag{4.4}$$

On substituting equations 4.1, 4.2 and 4.3 into 4.4 gives

$$\mathbf{x}^t + \mathbf{e}^a = \mathbf{W}(\mathbf{x}^t + \mathbf{e}^b) + \mathbf{K}(\mathbf{H}(\mathbf{x}^t) + \mathbf{e}^o) \tag{4.5}$$

The observation operator H is assumed to be linear so that $\mathbf{H}(\mathbf{x}^t) = H\mathbf{x}^t$. On applying the expectation operator on equation 4.5 and assuming errors are unbiased with $<\mathbf{e}^{\mathrm{o}}>$, $<\mathbf{e}^{\mathrm{b}}>$, $<\mathbf{e}^{\mathrm{a}}> = 0$ where $<>$ denote expectation operator gives equation 4.6. Details of the calculation can be referred to in Appendix A.

$$\mathbf{W} = \mathbf{I} - \mathbf{K}\mathbf{H} \tag{4.6}$$

On substituting equation 4.6 into equation 4.4, the following equation 4.7 for $\mathbf{x}^a$ is obtained.

$$\mathbf{x}^a = (\mathbf{I} - \mathbf{K}\mathbf{H})\mathbf{x}^b + \mathbf{K}\mathbf{y} \tag{4.7}$$

and hence

$$\mathbf{x}^a = \mathbf{x}^b + \mathbf{K}(\mathbf{y} - \mathbf{H}\mathbf{x}^b) \tag{4.8}$$

The matrix $\mathbf{K}$ is derived by substituting $\mathbf{x}^b$ from equation 4.1, $\mathbf{x}^a$ from equation 4.3 and $\mathbf{y}$ from equation 4.2 back into equation 4.8 and then computing the analysis error.

$$\mathbf{e}^a = \mathbf{e}^b(\mathbf{I} - \mathbf{K}\mathbf{H}) + \mathbf{K}\mathbf{e}^o \tag{4.9}$$

For the BLUE, the optimality condition corresponds to minimizing the trace of the analysis error given by

$$< \mathbf{e}^a \mathbf{e}^{aT} >= (\mathbf{I} - \mathbf{KH})\mathbf{B}(\mathbf{I} - \mathbf{KH})^T + \mathbf{KRK}^T \tag{4.10}$$

It can be seen in [73] that minimization of analysis error $< \mathbf{e}^a \mathbf{e}^{aT} >$ yields equation 4.11 for Kalman gain $\mathbf{K}$.

$$\mathbf{K} = \mathbf{BH}^T(\mathbf{HBH}^T + \mathbf{R})^{-1} \tag{4.11}$$

and also analysis error equation 4.12

$$\mathbf{A} = (\mathbf{I} - \mathbf{KH})\mathbf{B} \tag{4.12}$$

Equations 4.8, 4.11 and 4.12 constitute BLUE under the constraint of minimum variance [74].

4.3 Kalman filter

The Kalman filter is an algorithm that uses a series of measurements observed over time. These observations contain noise and other inaccuracies. The combination of model results and observations produce estimates of unknown variables that tend to be more precise than those based on observations alone [38]. A common application is for guidance, navigation and control of vehicles, particularly aircraft and spacecraft. Furthermore, the Kalman filter is a widely applied concept in time series analysis used in fields such as signal processing and econometrics [6].

When the state of system is dynamic instead of fixed, then there is a series of states $\mathbf{x}_k^t$, where k in subscript is a time index. It is assumed that initial state $\mathbf{x}_0^t$ and model errors are Gaussian distributed with mean $\mathbf{x}_0^b$ and noise covariance $\mathbf{Q}$. The Kalman filter is a sequential algorithm and works in two steps - predictor and corrector [74].

Predictor is responsible for projecting forward the current state and background error covariance matrix ($\mathbf{B}$). Herein, k+1 state and k+1 covariance estimates are predicted from the k state as can be seen in table 4.1. $\mathbf{Q}$ represents noise covariance which is typically very difficult to compute.

Corrector is responsible for feedback by incorporating observations to obtain an improved state estimate for the next predictor cycle. This is how the cycle of prediction and correction takes place to find an optimal solution. After each prediction and correction pair, the process is repeated with the new estimates used to initialize the model and the background error covariance. This recursive nature of Kalman filter makes implementation practical and feasible.

Table 4.1: Kalman filter with predictor equations to calculate $\mathbf{x}_{k+1}^a$ and $\mathbf{B}_{k+1}$

Kalman filter with predictor equations
$\mathbf{x}_{k+1}^a = \mathbf{A}_k\mathbf{x}_k^a + \mathbf{K}\mathbf{y}_k$
$\mathbf{B}_{k+1} = \mathbf{A}_k\mathbf{B}_k\mathbf{A}_k^T + \mathbf{Q}$

Table 4.2: Kalman filter with corrector equations to calculate $\mathbf{x}_k^b$, $\mathbf{x}_k^a$, $\mathbf{K}_k$ and $\mathbf{A}_k$

Kalman filter with corrector equations
$\mathbf{x}_k^b = \mathbf{x}_k^a$
$\mathbf{K}_k = \mathbf{B}_{k+1}\mathbf{H}^T(\mathbf{H}\mathbf{B}_{k+1}\mathbf{H}^T + \mathbf{R})^{-1}$
$\mathbf{x}_k^a = \mathbf{x}_k^b + \mathbf{K}_k(\mathbf{y}_k - H(\mathbf{x}_k^b))$
$\mathbf{A}_k = (\mathbf{I} - \mathbf{K}_k\mathbf{H})\mathbf{B}_{k+1}$

There are certain assumptions made while deriving the equations shown in table 4.1 and 4.2. Firstly, H operator is assumed to be linear. Secondly, the background error

covariance matrix ($\mathbf{B}$) and observation error covariance matrix ($\mathbf{R}$) should be positive definite. Thirdly, background and observations are assumed to be mutually uncorrelated and have unbiased errors [73]. Fourthly, in this thesis $\mathbf{B}$ is assumed to be static and is precomputed before applying data fusion.

4.4 Optimal interpolation (OI)

Optimal interpolation (OI) is an alternative implementation of equation 4.8 which uses a simplified version of BLUE, given by equation 4.11, to find the analysis over a small region. The main assumption in OI is that for each background state only a few observations surrounding it are important because it is only these observations that have the effect on the analysis, while observations at a distant location have little impact. So, for each $\mathbf{x^b}$ a set of observations surrounding it are selected by drawing a box around it. It is this box which defines the region of computation. All observations in this box are then used to compute parameters for the data assimilation. Mentioned parameters include H_m(observation operator), $H_m(\mathbf{x}^{\mathrm{b}})$(state mapped to m observation space) and $\mathbf{R}_m$(observation error covariance). Also, here m represents the number of observations in the new defined domain of the box.

In figure 4.2 a grid defining the region of study as a box is used. Here red stars represent observations and green pixel is the background variable, the black box is the domain under study and the green box is an analysis box i.e. new domain of study for the current background state.

To calculate the analysis for green pixel, equations 4.13 and 4.14 are used and they use all the observations in the analysis green box only.

$$\mathbf{K}_m = \mathbf{B}\mathbf{H}_m^T(\mathbf{H}_m\mathbf{B}\mathbf{H}_m^m + \mathbf{R}_m)^{-1} \tag{4.13}$$

$$\mathbf{x}^a = \mathbf{x}^b + \mathbf{K}_m(\mathbf{y}_m - H_m(\mathbf{x}^b)) \tag{4.14}$$

where

- $\mathbf{y}_m$ observations in the analysis box, (m times)
- H_m - observation operator in the analysis box space, (m times n)
- $\mathbf{R}_m$ - observation error covariance matrix in the analysis box , (m times m)

An example is provided below. In Figure 4.2, it is assumed that there are 1000 observations and 100 background states. All computations have to be done on 100 background states such that $H(\mathbf{x}^b)$ and $\mathbf{R}$ are (1000 times 100) and (1000 times 1000) respectively for BLUE with Kalman Filter method. Now a square green box is defined, such that there are 30 observations in the box. The selection of the analysis box should be such that it takes into consideration all observations which might have significant effect. For applying OI, H_m and $\mathbf{R}_m$ becomes a matrix of dimensions (1000 times 30) and (30 times 30) respectively. It is very useful as it reduces the size of calculation significantly, primarily because the size of the matrix that is to be inverted is as small as 30 times 30.

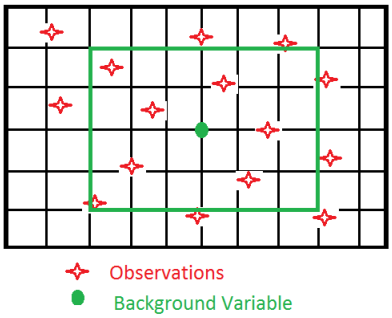

Figure 4.2: OI data selection by drawing a green box around green dot observations so that all red star observations are used in computation

The advantage of OI is its simplicity of implementation and it's relatively low cost. A drawback of OI is that spurious noise is produced in the analysis fields because different sets of observations are used in different parts of the model [73]. In addition, as only a local set of observations are used, the estimates are not optimal in the global sense.

4.5 Summary

This chapter defines data assimilation and explain its techniques. It presented BLUE, Kalman filter and optimal interpolation. The following chapter explains how various parameters i.e. background error covariance matrix ($\mathbf{B}$), observation operator (H) and observation error covariance matrix ($\mathbf{R}$) are computed to apply the data assimilation technique and present results for applying this technique with AMSR-E observations. It also applies this technique to estimate ice thickness and then uses these estimates of ice thickness to calculate routes for ship navigation through the Arctic region in the framework of a toy example.

Chapter 5

Results and Discussion

This chapter is divided into three sections. The first section, 5.1, describes the computation of **B** - background covariance matrix, H - observation operator, **R** - observation error covariance matrix and discusses the method chosen to obtain the analysis. The second section, 5.2, contains three subsections which show results from changing the value of the observation error standard deviation σ_o, the impact of saturation of H on ice thickness and comparison of results from data fusion using AMSR-E data for the month of January 2007. The last section in this chapter is the application of data assimilation and is used to find the optimal path for ships to route through ice covered water.

5.1 Parameter Computation

The first step in the mathematical formulation of the analysis problem is the definition of the region of study. The area chosen for the study is the Labrador coast, which is along the east coast of Canada. There are two inputs to the data fusion method, one is the

background state ($\mathbf{x}^{\mathrm{b}}$) and other is the observation ($\mathbf{y}$). The background state represents the ice thickness over the area of study, and is explained in section 3.1. The observations y is from remote sensing data, described in section 3.2 and 3.3.

The next step would be parameter computation, section 5.1 describes the method used to compute the background error covariance matrix ($\mathbf{B}$), the observation error covariance matrix ($\mathbf{R}$) and the observation operator (H).

5.1.1 B - Background error covariance matrix

The background error is defined as the difference between the background state and the true state of $\mathbf{x}$, $\mathbf{e}^{\mathrm{b}} = \mathbf{x}^{\mathrm{b}}$ - $\mathbf{x}^{\mathrm{t}}$. The background error covariance matrix is defined as $\mathbf{B} =< \mathbf{e}^{b}(\mathbf{e}^{b})^{T} >$, where <> denotes an average over many realizations. This matrix can be static, meaning that it does not evolve with the state or it can be state dependent. For the ice thickness fusion carried out in this thesis it is assumed to be static. The diffusion operator is used to calculate background error covariance matrix mainly for three reasons (a) the resulting function is positive definite, (b) it is computationally inexpensive and (c) it can control homogeneity and isotropy [75].

The diffusion operator (q) performs the spatial spreading of information from the observation point to the surrounding domain [66]. In this thesis, the diffusion operator q is calculated by solving the diffusion equation at each point in the background state. The diffusion equation is a partial differential equation (PDE) which describes the density dynamics in a material undergoing diffusion. For example, consider one meter thick ice on any point in the background state, then the diffusion equation describes how this thickness will spread and how many other locations in the background state are affected by it. Equation 5.1 is the diffusion equation in 2 dimensions where α is the diffusivity constant

and ϕ is any scalar field as a function of time and space.

$$\frac{\partial \boldsymbol{\phi}}{\partial t} = \boldsymbol{\alpha}\left(\frac{\partial^2 \boldsymbol{\phi}}{\partial u^2} + \frac{\partial^2 \boldsymbol{\phi}}{\partial v^2}\right) + Source \tag{5.1}$$

Here

- $\boldsymbol{\phi}(u, v, t)$ is the scalar field function of time and space
- t is the time
- u is the coordinate in the zonal (east - west) direction
- v is the coordinate in the meridional (north - south) direction
- α is the diffusion coefficient

The partial differential equation (PDE) can be solved by either an implicit or explicit method [76]. An implicit method requires the current system state and also the system state at a later point in time. The solution is converged iteratively. To solve equation 5.1 by implicit method, apply the backward difference on the left side of equation 5.1 and the second order central difference on the right side of equation 5.1, then equation 5.2 is obtained. The source term represents the generation of the scalar that is undergoing diffusion.

$$\frac{\boldsymbol{\phi}_{i,j}^{nt+1} - \boldsymbol{\phi}_{i,j}^{nt}}{\boldsymbol{\Delta} t} = \boldsymbol{\alpha}\left(\frac{\boldsymbol{\phi}_{i,j+1}^{nt+1} - 2\boldsymbol{\phi}_{i,j}^{nt+1} + \boldsymbol{\phi}_{i,j-1}^{nt+1}}{\boldsymbol{\Delta} u^2} + \frac{\boldsymbol{\phi}_{i+1,j}^{nt+1} - 2\boldsymbol{\phi}_{i,j}^{nt+1} + \boldsymbol{\phi}_{i-1,j}^{nt+1}}{\boldsymbol{\Delta} v^2}\right) + Source(i, j) \tag{5.2}$$

where

- i is one step in the zonal direction
- j is one step in the meridional direction

- nt is the previous time level
- nt + 1 is the current time level

Equation 5.2 can be rearranged to obtain equation 5.3

$$(\frac{\boldsymbol{\alpha}\Delta t}{\Delta u^2})\boldsymbol{\phi}_{i+1,j}^{nt+1} + (\frac{\boldsymbol{\alpha}\Delta t}{\Delta u^2})\boldsymbol{\phi}_{i-1,j}^{nt+1} + (\frac{\boldsymbol{\alpha}\Delta t}{\boldsymbol{\Delta} v^2})\boldsymbol{\phi}_{i,j+1}^{nt+1} + (\frac{\boldsymbol{\alpha}\Delta t}{\boldsymbol{\Delta} v^2})\boldsymbol{\phi}_{i,j-1}^{nt+1} = (1 + 2\frac{\boldsymbol{\alpha}\Delta t}{\boldsymbol{\Delta} u^2} + 2\frac{\boldsymbol{\alpha}\Delta t}{\boldsymbol{\Delta} v^2})\boldsymbol{\phi}_{i,j}^{nt+1} + \boldsymbol{\phi}_{i,j}^{nt} + \boldsymbol{\Delta} t Source(i,j) \quad (5.3)$$

In equation 5.3 it is seen that to find $\boldsymbol{\phi}_{i+1,j}^{nt+1}, \phi_{i-1,j}^{nt+1}, \phi_{i,j+1}^{nt+1}, \phi_{i,j-1}^{nt+1}$ and $\boldsymbol{\phi}_{i,j}^{nt+1}$ we would need to solve the problem iteratively. When the implicit method was used for the present study, it did not converge at few points and hence was not investigated further.

The explicit method calculates the system state at the current time step using information from the previous time step. At each node, the explicit method is applied by using the backward difference on the left side of equation 5.1 and the second order central difference on the right side of equation 5.1, obtaining equation 5.4.

$$\frac{\boldsymbol{\phi}_{i,j}^{nt+1} - \boldsymbol{\phi}_{i,j}^{nt}}{\boldsymbol{\Delta} t} = \boldsymbol{\alpha}(\frac{\boldsymbol{\phi}_{i,j+1}^{nt} - 2\boldsymbol{\phi}_{i,j}^{nt} + \boldsymbol{\phi}_{i,j-1}^{nt}}{\boldsymbol{\Delta} u^2} + \frac{\boldsymbol{\phi}_{i+1,j}^{nt} - 2\boldsymbol{\phi}_{i,j}^{nt} + \boldsymbol{\phi}_{i-1,j}^{nt}}{\boldsymbol{\Delta} v^2}) + Source(i,j) \quad (5.4)$$

$$\boldsymbol{\phi}_{i+1,j}^{nt+1} = (\frac{\boldsymbol{\alpha}\Delta t}{\boldsymbol{\Delta} u^2})\boldsymbol{\phi}_{i+1,j}^{nt} + (\frac{\boldsymbol{\alpha}\Delta t}{\boldsymbol{\Delta} u^2})\boldsymbol{\phi}_{i-1,j}^{nt} + (\frac{\boldsymbol{\alpha}\Delta t}{\boldsymbol{\Delta} v^2})\boldsymbol{\phi}_{i,j+1}^{nt} + (\frac{\boldsymbol{\alpha}\Delta t}{\boldsymbol{\Delta} v^2})\boldsymbol{\phi}_{i,j-1}^{nt} + (1 - 2\frac{\boldsymbol{\alpha}\Delta t}{\boldsymbol{\Delta} u^2} + 2\frac{\boldsymbol{\alpha}\Delta t}{\boldsymbol{\Delta} v^2})\boldsymbol{\phi}_{i,j}^{nt} + \boldsymbol{\Delta} t Source(i,j) \quad (5.5)$$

The explicit method is generally unstable and requires small time steps, while an implicit method is unconditionally stable and can use larger time steps. To study the stability of the explicit method, Von Neumann stability analysis is used [23]. A system is said to

be stable if errors do not increase over the iteration of computations. To solve diffusion equation explicitly, Δt should be given by equation 5.6 to obtain a bounded solution.

$$\Delta t = \frac{min(\Delta u^2, \Delta v^2)}{4\alpha} \tag{5.6}$$

When solving equation 5.5 boundary conditions need to be applied. The coast represents the land boundary. Since there is no sea ice on land, a boundary condition enforcing a value of zero on the coast is applied, which corresponds to a homogeneous Dirichlet boundary condition. A Dirichlet boundary condition specifies the value a solution needs to take on the boundary of the domain [77]. For, the other boundary i.e. the open ocean, a Neumann boundary condition is applied. The Neumann boundary condition specifies the value that the derivative of a solution should take on the boundary of the domain [77]. Equation 5.7 and 5.8 shows equations for Dirichlet and Neumann boundary conditions respectively.

$$\boldsymbol{\phi}_{i+1,j}^{nt+1} = \boldsymbol{\phi}_{i,j}^{nt} \tag{5.7}$$

$$\boldsymbol{\phi}_{i+1,j}^{nt+1} = \boldsymbol{\phi}_{i,j}^{nt} + \boldsymbol{\Delta} tSource(i,j) \tag{5.8}$$

It is known that solving the diffusion equation with an explicit method is conditionally stable if the size of the time step is limited [78]. Comparison by Matthew [78] shows that implicit and explicit correlation operators give results similar in magnitude, shape and spatial size.

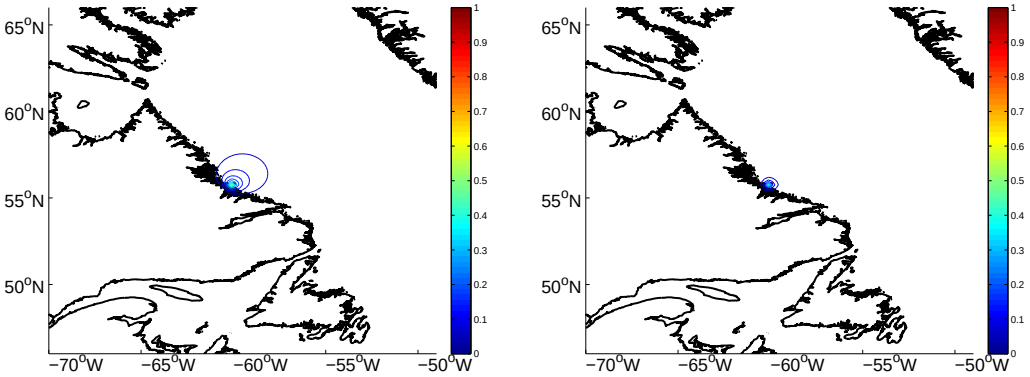

(a) Diffusion at coast with Ld = 5 units

(b) Diffusion at coast with Ld = 2 units

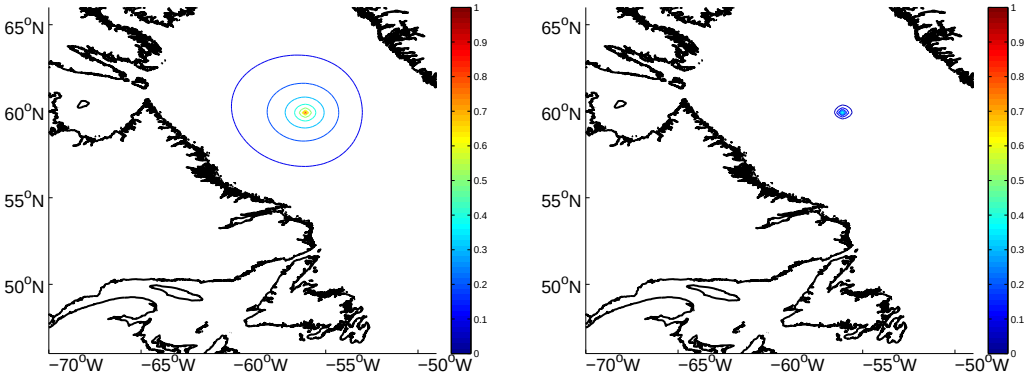

(c) Diffusion away from the coast with Ld = 5 units

(d) Diffusion away from the coast with Ld = 2 units

Figure 5.1: Contour of diffusion operator q for a single background state at coast and away from the coast with a different diffusion length scale. Elliptical circles are closer at boundary and becomes more diffused on moving away from the coast while length of diffusion is controlled by diffusion length.

The diffusion of ϕ can be limited by changing the length scale of diffusion, which is given by equation 5.9 where T is diffusion time [79]. The diffusion length scale is directly

proportional to time and the diffusion coefficient α. For our thesis, α is considered as constant and diffusion time was varied to change the diffusion length scale.

$$Ld = \sqrt{4\alpha T} \tag{5.9}$$

Figure 5.1 shows the contour of the diffusion equation at a boundary node and at an interior node with a different diffusion length scale. The effect of diffusion is represented by elliptical circles. It can be seen that when Ld is chosen to be very small, only a small region surrounding the source is affected. Figures 5.1a and 5.1b, and figures 5.1c and 5.1d, display the diffusion of scalar on the coast and away from the coast respectively. At the boundary, elliptical circles are closer and become more diffuse when moving away from the coast, while in the sea elliptical circles are uniformly spread out.

Each row in the diffusion operator q is the solution of the diffusion equation computed at a given node on the grid. If a model has n background states then q has dimension n times n.

Computation of background error covariance matrix with the diffusion operator and its normalization is explained in Appendix B.

5.1.2 H - Observation operator

In data fusion two different data sets are combined: the background state and the observations. It is not necessary that they are comparable in terms of resolution or region of study. An operator is used to map the background state to the observation space. This operator is called the observation operator and is denoted by H.

H(x) may be simple interpolation from model grid to observation locations or a complex non-linear function, or a combination of linear and non-linear functions.

For example, if both observations and background state are ice thickness valid over the same range of thickness values, then H can be an operator that simply interpolates the state to the observation locations. In the thesis, we use bilinear interpolation method to interpolate the state to observation location. The key idea of bilinear interpolation is to perform interpolation in one direction and then again in the other direction.

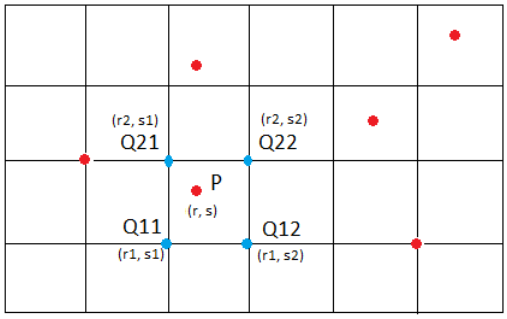

Figure 5.2: Grid for bilinear interpolation where blue dots are model state and red dots are observations

Assume that in figure 5.2, the blue dots are background state and the red dots are observations. The value of background state at four points Q11(r1,s1), Q12(r1,s2), Q21(r2,s1) and Q22(r2,s2,) is given by ${x^b}_{11}, {x^b}_{12}, {x^b}_{21}$ and ${x^b}_{22}$. P(x,y) represents the observation location for which bilinear interpolation is to be applied. The latitude and longitude coordinates for background state are r1, r2 and s1, s2, while r and s are latitude and longitude coordinates for the observation.

Applying bi-linear interpolation gives

$$H(x) = f_1 {x^b}_{11} + f_2 {x^b}_{12} + f_3 {x^b}_{21} + f_4 {x^b}_{22} \tag{5.10a}$$

$$f_1 = \frac{(r2 - r)(s2 - s)}{(r2 - r1)(s2 - s1)} \tag{5.10b}$$

$$f_2 = \frac{(r2 - r)(s - s1)}{(r2 - r1)(s2 - s1)} \tag{5.10c}$$

$$f_3 = \frac{(r - r1)(s2 - s)}{(r2 - r1)(s2 - s1)} \tag{5.10d}$$

$$f_4 = \frac{(r - r1)(s - s1)}{(r2 - r1)(s2 - s1)} \tag{5.10e}$$

This thesis uses ice thickness observations from AMSR-E and MODIS sensors, which have an upper threshold to the ice thickness they can measure. AMSR-E cannot measure ice thickness greater than 0.2 m while MODIS cannot measure ice thickness greater than 0.5 m, as discussed earlier in sections 3.2 and 3.3. Hence, all interpolated values above 0.2 m for AMSR-E and 0.5 m for MODIS should be saturated to their threshold values. For all values of ice thickness less than threshold, a linear forward model is applied, while all values of ice thickness more than the threshold are saturated to their threshold values.

$$H(x) = \begin{cases} \text{linear forward model, ice thickness} \leq \text{threshold} \\ \text{saturation function, ice thickness} > \text{threshold} \end{cases}$$

For example, assume that x^b_{12} and x^b_{21} are more than the threshold value and x^b_{11} and x^b_{22} are both less than the threshold value, then H(x) is

$$H(x) = f_1 x^{\mathrm{b}}{}_{11} + f_2 H_{sat}(x^{\mathrm{b}}{}_{12}) + f_3 H_{sat}(x^{\mathrm{b}}{}_{21}) + f_4 x^{\mathrm{b}}{}_{22} \tag{5.11}$$

where the saturation function for AMSR-E and MODIS are given by,

$$H_{sat}(x^b) = Th - (\frac{log(M + e^{-N(x^b - Th)}}{N}) \tag{5.12}$$

and

- Th - Threshold 0.2 for AMSR-E and 0.5 for MODIS
- M and N are constants

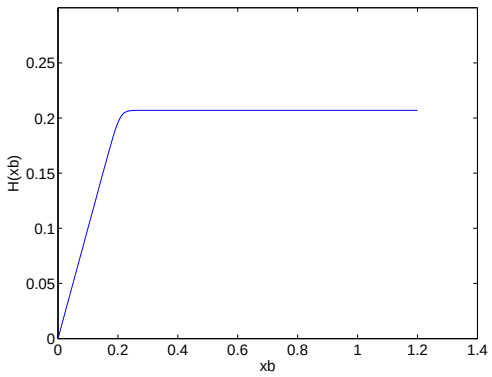

(a) Saturation function for AMSR-E

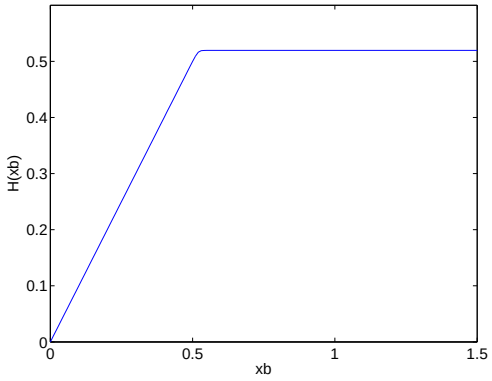

(b) Saturation function for MODIS

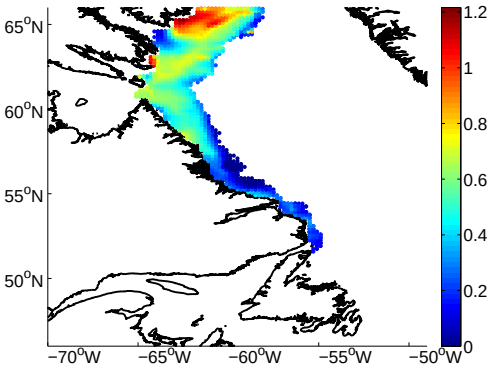

(c) $H(x^b)$ without saturation for AMSR-E

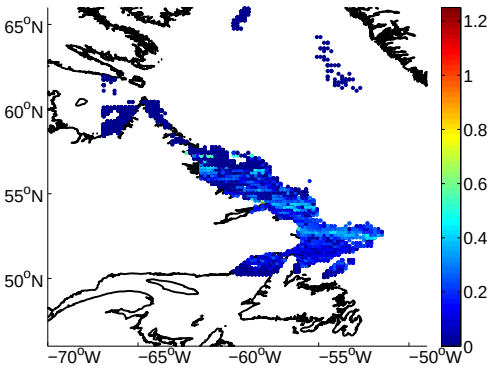

(d) $H(x^b)$ without saturation for MODIS

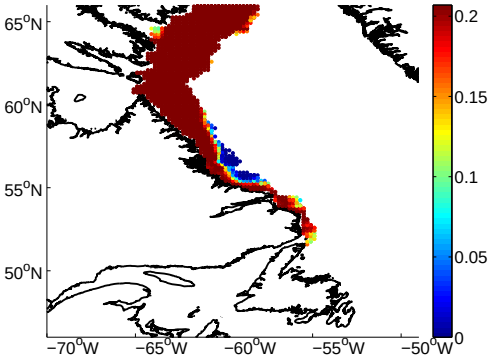

(e) $H(x^b)$ with saturation for AMSR-E

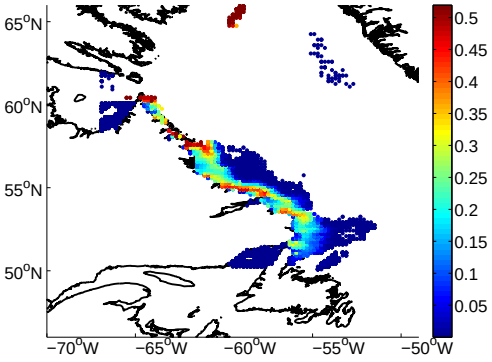

(f) $H(x^b)$ with saturation for MODIS

Figure 5.3: $H(x^b)$ for ice thickness from January 24, 2007. Panels (a) and (b) shows function $H(x^b)$ for AMSR-E and MODIS which is saturated at 0.2m and 0.5m respectively. Panels (c) and (d) shows not saturated $H(x^b)$ and have values more than threshold while panels (e) and (f) are saturated $H(x^b)$.

These functions, $H_{sat}(x^b)_{AMSR-E}$ and $H_{sat}(x^b)_{MODIS}$, are shown in figure 5.3a and 5.3b respectively for $H(\mathbf{x}^b)$ versus $\mathbf{x}^b$. In future different functions can be used to examine the impact of $H(\mathbf{x}^b)$. On comparing figure 5.3c and 5.3e it is observed that all values of $H(x^b)$ more than 0.2 m are saturated and are limited to the upper threshold of 0.2 m. Similarly, on comparing figure 5.3d and 5.3f it is observed that all values of $H(x^b)$ more than 0.5 m are saturated and are limited to the upper threshold of 0.5 m.

In the data fusion the Jacobian of H is also needed. This is $\mathbf{H} \approx \frac{\partial H}{\partial x}$ as is given in equation 5.13. Here $H_1(x)$, $H_2(x)$ are $\mathbf{H(x)}$ for observations 1 and 2 calculated using equation 5.10 and x^b_{11}, x^b_{12} are background states.

$$\mathbf{H} = \begin{bmatrix} \frac{\partial H_1(x)}{\partial x^b_{11}} & \frac{\partial H_1(x)}{\partial x^b_{12}} & \dots & \frac{\partial H_1(x)}{\partial x^b_{21}} & \frac{\partial H_1(x)}{\partial x^b_{22}} \dots \\ \frac{\partial H_2(x)}{\partial x^b_{11}} & \frac{\partial H_2(x)}{\partial x^b_{12}} & \dots & \frac{\partial H_2(x)}{\partial x^b_{21}} & \frac{\partial H_2(x)}{\partial x^b_{22}} \dots \\ \dots & \dots & \dots & \dots & \dots & \dots \end{bmatrix} \tag{5.13}$$

From equation 4.8 it is seen that analysis largely depends on the difference between observations and the background values in the observation space when the Kalman gain $\mathbf{K}$ is a constant. Figure 5.4 shows the innovation for AMSR-E and MODIS observations when saturation is used. The innovation is the difference between the observation vector and the transformed background estimate, $\mathbf{y} - H(\mathbf{x}^b)$.

It can be seen that the innovation for AMSR-E is mostly green which is zero. The background thickness is overestimated for a few regions along the Labrador coast along (-60 °W and 55 °N) and is underestimated in the Hudson Strait along (-65 °W and 60 °N). For MODIS most of the region is blue with zero or 0.1 m innovation. The background state thickness is underestimated relative to observations along (-60 °W and 57 °N). It can be seen there is a yellow orange discontinuous pattern over the open ocean in figure 5.4b that may be due to clouds that were not detected by the cloud mask.

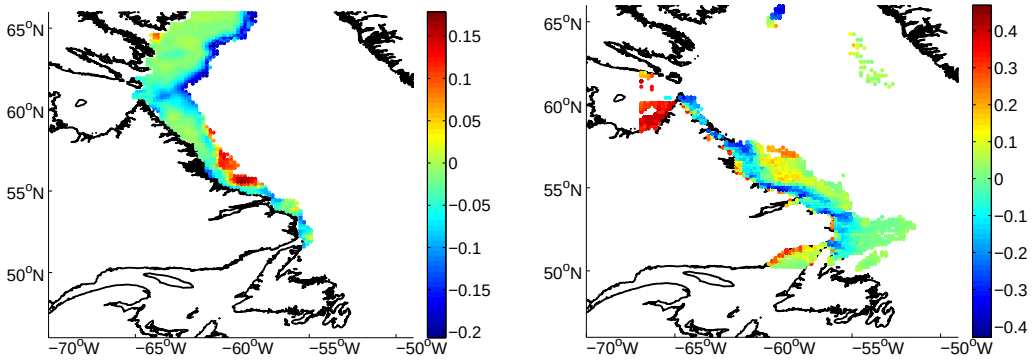

(a) Innovation for AMSR-E

(b) Innovation for MODISS

Figure 5.4: ($\mathbf{y}$ - H(x^b)) - Innovation for observing system with saturation applied to the H operator. It shows how much observations differ from the interpolated model values.

5.1.3 R - Observation error covariance matrix

The observation error covariance matrix, $\mathbf{R}$, represents error in the observational process which can be due to the following sources.

- Instrument error can be due to errors in the observing platform or instruments. The instruments used may not be precise in readings and hence often contribute to some errors in the measurement.
- Representativity errors can arise when observation locations do not correspond exactly to the region under study or when the observations contain scales not represented in the background state. This can happen when the sea ice model and observations have different spatial resolutions. In addition, some errors occur when interpolating the state vector to the observation space.
- Synoptic error occurs when all observations are not taken at the same time, but are

treated in the data assimilation system as though they have the same valid time.

It is typically assumed that the observation error covariance matrix, $\mathbf{R}$, is diagonal because observations with complicated observation errors can be difficult to assimilate. When $\mathbf{R}$ is diagonal it has the form, $\mathbf{R} = \sigma_o^2 I$, where σ_o^2, is the observation error standard deviation. Section 5.2.1 discusses how changing the values of σ_o affects the analysis.

5.1.4 Method used for analysis

To obtain analysis state the combination of BLUE and Kalman filter equations, as shown in equation 4.11 and 4.8, is used. The background state and observations are combined by these equations to produce estimated analysis states. The model has a spatial resolution of 1/5°in longitude and 1/6°in latitude which leads to 5119 points in the solution domain. To analyse this method, a clear day of January 24, 2007 is used with 4,000 AMSR-E and 40,000 MODIS observations. On rewriting equation 4.11 and 4.8 with the dimension of each vector and matrix involved gives

$$\underbrace{\mathbf{K}}_{(5119*4000)or(5119*40000)} = \overbrace{\underbrace{\mathbf{B}\mathbf{H}^T}}^{(5119*4000)or(5119*40000)} \underbrace{(\mathbf{H}\mathbf{B}\mathbf{H}^T + \mathbf{R})^{-1}}_{(4000*4000)or(40000*40000)} \tag{5.14}$$

$$\mathbf{x}^a = \underbrace{\mathbf{x}^b}_{5119*1} + \mathbf{K} \underbrace{(\mathbf{y} - \mathbf{H}(\mathbf{x}^b)}_{(4000*1)or(40000*1)}) \tag{5.15}$$

In equation 5.14 and 5.15 4000 refers to AMSR-E and 40000 to MODIS observations. It is also observed in equation 5.14 that inverse of matrix of dimension 4000 * 4000 or 40000 * 40000 is involved. This computation is very time consuming.

Optimal interpolation is a method in which the problem of large matrix inversion is successfully overcome. A premise in OI is that impact of each observation is limited in spatial extent. OI solves BLUE equations on a small domain surrounding the background state. A small box is drawn around each state variable to take only the observations inside this box to estimate the sea ice thickness. Hence, it was concluded that optimal interpolation is best for the study because it comparatively consumes less time and provides an optimal solution to our problem.

5.2 Ice Thickness Results

The first section, 5.2.1, shows how changing the observation error standard deviation will affect the analysis estimates. In the second section, 5.2.2, it is shown how applying saturation to the forward model improves the ice thickness estimates. In section, 5.2.3, estimates from fusing AMSR-E data with ice thickness from a model for the month of January 2007 are presented. All experiments in this section are compared to ice charts for verification.

5.2.1 Effect of changing the observation error standard deviation

The observation error standard deviation, σ_o, contains error in the observational process that could be due to instruments, representation, synoptic error or other errors, such as human error, transmission error or malfunctioning of instrument.

To explore the observation error covariance matrix $\mathbf{R}$, the errors in the ice thickness from AMSR-E and MODIS have been computed using the triple collocation method as explained in [2]. This method assumes that each observation is linearly related to the true state. The error associated with ice thickness from AMSR-E data was much lower

than that for ice thickness from MODIS data when thickness values for January 2007 was considered. Also some of the MODIS ice thickness values are very large due to clouds that have been mistaken for sea ice. These large values need to be identified and removed before data fusion.

The impact of using different values of σ_o is shown in figures 5.5, 5.6 and 5.7. In 5.5 it is seen that changing the value of σ_o from 0.2 to 0.03 changes the analysis increment as shown in figure 5.5e and 5.5c. This shows how the ice thickness pattern changes over the thin ice edge. It is observed that the analysis increment is continuous along the ice edge with $\sigma_o = 0.03$ and is discontinuous with $\sigma_o = 0.2$. Also, the analysis for $\sigma_o = 0.03$ takes away ice at a few places (-60 °W, 64 °N) because the observation from AMSR-E satellite is more than the ice ocean model estimate. Hence, it improves analysis by estimating values closer to observations as can be seen in figure 5.5f and 5.5d.

Figure 5.6 shows how the same value of $\sigma_o = 0.2$ gives different results for a different set of observations. When AMSR-E observations are used the analysis increment in figure 5.6c is not as continuous over the thin ice edge as for AMSR-E because it requires σ_o to be much lower than 0.2. MODIS analysis increment in figure 5.6e is quite distributed over the domain with more continuous distribution over thin ice edges. Thus it is concluded that AMSR-E and MODIS need different values of $\mathbf{R}$ to be used in data assimilation.

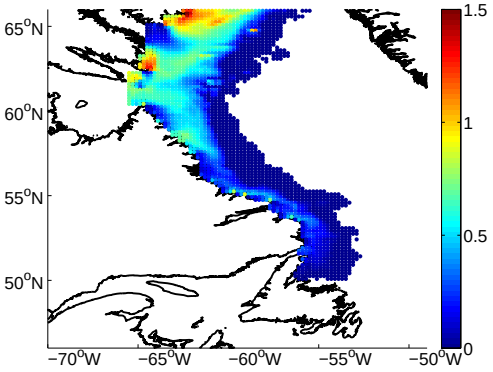

(a) Background state x^b

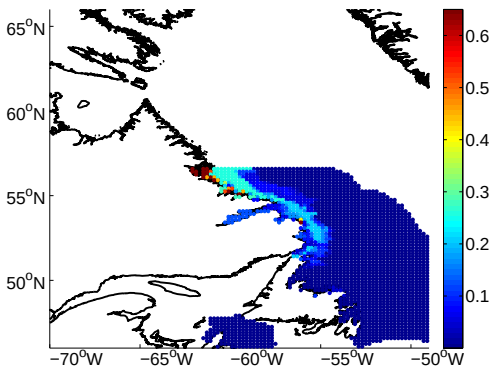

(b) Ice Chart Data

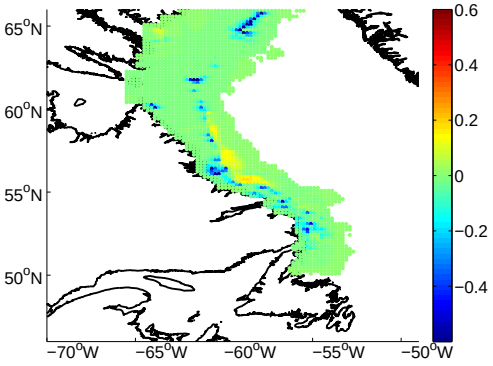

(c) Analysis increment for AMSR-E with $\sigma_o = 0.03$ standard deviation

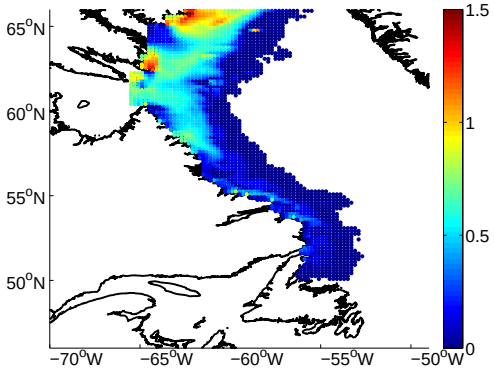

(d) Analysis for AMSR-E with $\sigma_o = 0.03$ standard deviation

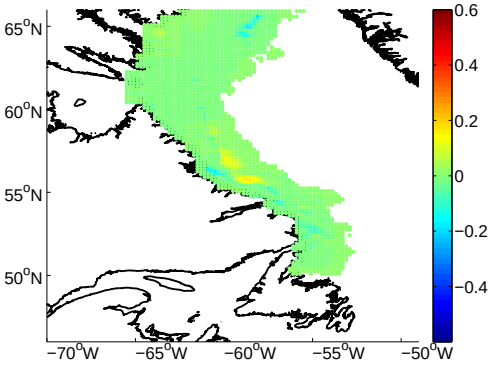

(e) Analysis increment for AMSR-E with $\sigma_o = 0.2$ standard deviation

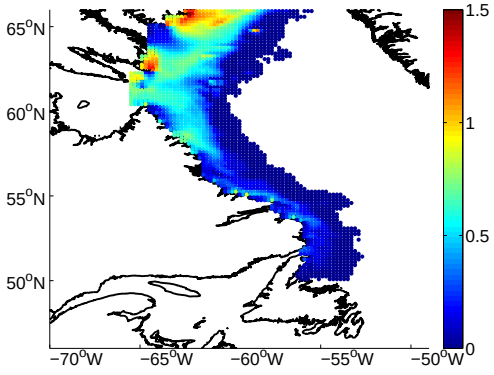

(f) Analysis for AMSR-E with $\sigma_o = 0.2$ standard deviation

Figure 5.5: AMSR-E data for January 24, 2007 with σ_o, 0.03 and 0.2, shows that Aanalysis increment used is more continuous in panels (c) than (e) and also estimates for panel (d) is better than panel (f).

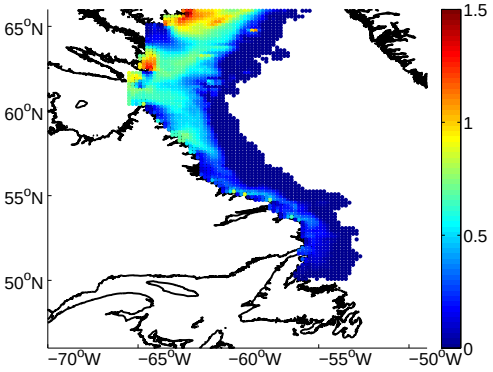

(a) Background state x^b

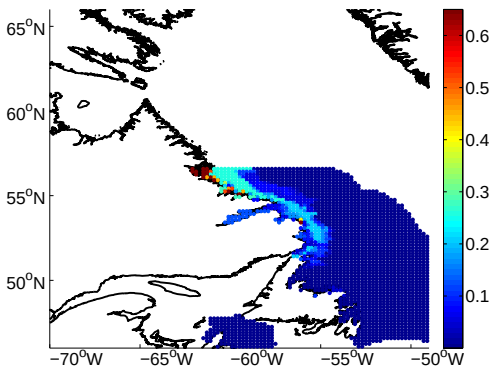

(b) Ice Chart Data

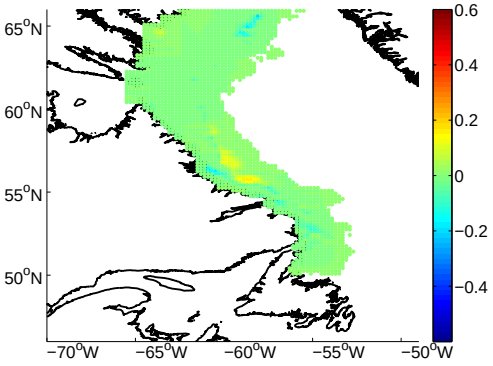

(c) Analysis increment for AMSR-E with $\sigma_o = 0.2$ standard deviation

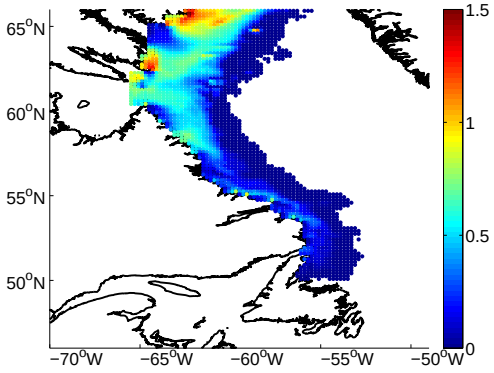

(d) Analysis for AMSR-E with $\sigma_o = 0.2$ standard deviation

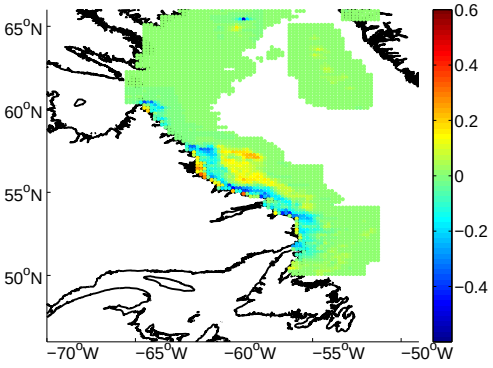

(e) Analysis increment for MODIS with $\sigma_o = 0.2$ standard deviation

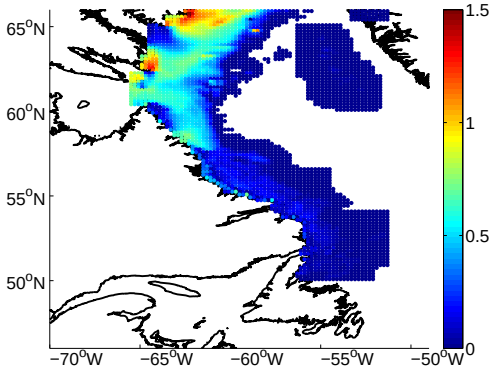

(f) Analysis for MODIS with $\sigma_o = 0.2$ standard deviation

Figure 5.6: Effect of using $\sigma_o = 0.2$ for both AMSR-E and MODIS observations for January 24, 2007. Panels (c) and (e) shows different pattern in analysis increment due to different set of observations used.

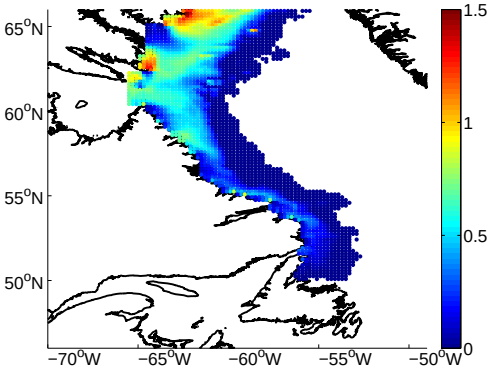

(a) Background state x^b

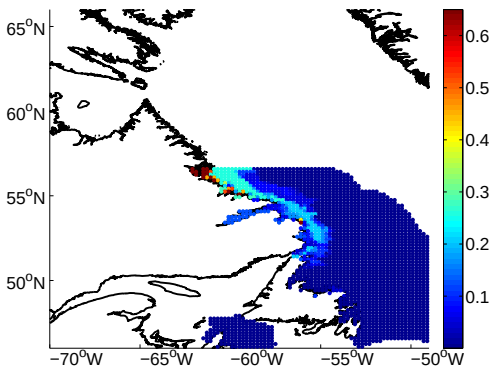

(b) Ice Chart Data

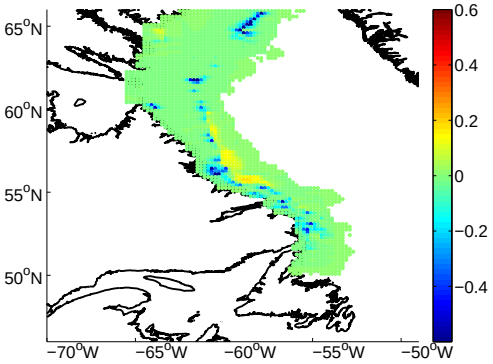

(c) Analysis increment for AMSR-E with $\sigma_o = 0.03$ standard deviation

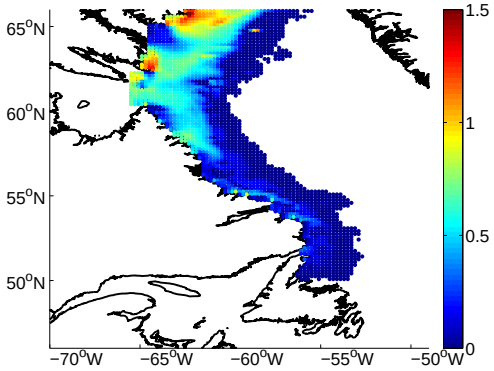

(d) Analysis for AMSR-E with $\sigma_o = 0.03$ standard deviation

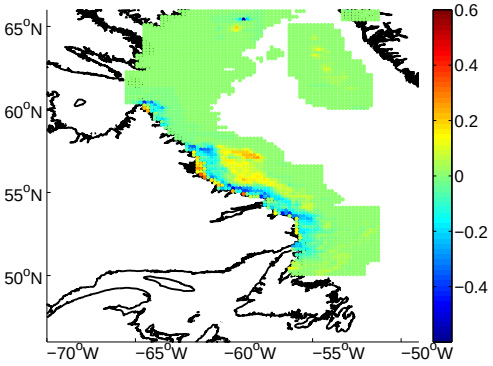

(e) Analysis increment for MODIS with $\sigma_o = 0.15$ standard deviation

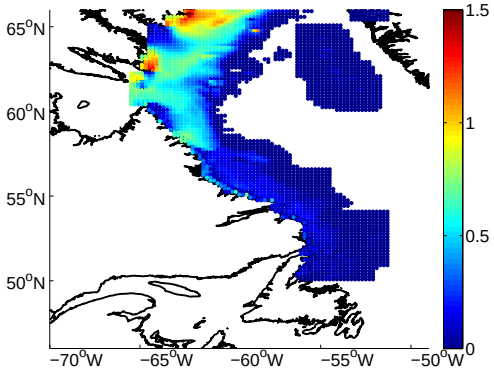

(f) Analysis increment for MODIS with $\sigma_o = 0.15$ standard deviation

Figure 5.7: Effect of using $\sigma_o = 0.03$ for AMSR-E and $\sigma_o = 0.15$ for MODIS from [2] for January 24, 2007

Figure 5.7 shows how different values of σ_o with a different set of observations provide a good analysis. As per different experiments done with different values of σ_o and also referring to [2], it was concluded that $\sigma_o = 0.03$ for AMSR-E and $\sigma_o = 0.2$ for MODIS provides good analysis results as shown in figure 5.7d and 5.7f.

Table 5.1: Means and standard deviations for the difference between estimated ice thickness and CIS ice data for January 24, 2007 demonstrating the impact of changing observation error standard deviation (σ_o) values

Experiment	Observation error Standard deviation	Mean Analysis - Ice Charts (m)	Standard deviation Analysis - Ice Charts (m)	Mean Background - Ice Charts (m)	Standard deviation Background - Ice Charts (m)
Case 1 with MODIS	0.2	0.0096	0.0727	0.0084	0.0727
Case 2 with AMSR-E	0.2	0.0070	0.0728	0.0084	0.0727
Case 3 with MODIS	0.15	0.0099	0.0728	0.0084	0.0727
Case 4 with AMSR-E	0.03	0.0001	0.0830	0.0084	0.0727

Means and standard deviations of the differences in ice thickness values from data fusion and ice charts were computed in order to validate results. Table 5.1 shows how changing the value of observation error standard deviation σ_o, given in the second column of table, affects the mean and the standard deviation regarding the difference between estimated ice thickness and that based on CIS ice charts when AMSR-E and MODIS observations

are used. The smaller the value of the mean, the closer it is to the charts. $\sigma_o = 0.2$ gives the mean of difference between ice thickness estimation and ice charts as 0.0055 m for AMSR-E and 0.0096 m for MODIS. Changing σ_o with a decrease in magnitude of 0.17 m, as per Scott [2], reduces the bias and standard deviation of the difference between the analysis and the ice charts for the case when AMSR-E data is used. However, for MODIS a change in σ_o by a magnitude of 0.05 did not bring any appreciable change in the mean and standard deviation. Keeping in view, the very low values of the aforementioned means and standard deviations it can be concluded that data fusion technique is producing results close to ice charts with $\sigma_o = 0.03$ for AMSRE while for MODIS analysis is worse than ice charts. It was found by visual inspection of the results that the MODIS data has too many gross errors due to unmasked clouds.

5.2.2 Effect of observation operator with and without saturation

The observation operator (denoted as H) produces a model equivalent of the observation needed to enable comparison between the state and the observations in observation space. This section shows ice thickness estimates using both AMSR-E and MODIS data computed under the conditions with and without saturation of the observation operator.

MODIS Ice Thickness Results

Results for estimated ice thickness are shown in Figure 5.8 with the background state and observations shown in figures 5.8a and 5.8b respectively. This section has two sets of estimates, one without saturation and the other with saturation.

When threshold of 0.5 m is applied to the fusion method by limiting the model equivalent of observations to saturation level, then $\mathrm{H}(\mathbf{x}^{\mathrm{b}})$ changes from figure 5.3d to figure 5.3f.

All values of $H(\mathbf{x}^b)$ above 0.5 m are masked to saturation level. The analysis figures 5.8f and 5.8d and increment figures 5.8e and 5.8c does not show much change after applying saturation to H operator. It is because all MODIS observations for this day have thickness value less than 0.5 m and hence no saturation is needed to mask MODIS observations.

AMSR-E Ice Thickness Results

Results for estimated ice thickness are shown in Figure 5.9 with the background state and observations shown in figures 5.9a and 5.9b respectively. This section has two sets of estimates: one without saturation and the other with saturation.

AMSR-E estimate for sea ice thickness without saturation is shown in Figure 5.9d. These estimates when compared with the background state in Figure 5.9a look incorrect as in that ice thickness is significantly below what is expected for January. Figure 5.3c shows that model equivalent of observations, $H(\mathbf{x})$, without saturation. Values greater than 0.2 m can be seen, which is incorrect because AMSR-E sensors can measure ice up to 0.2 m only. Hence, there is the need to correct observation operator by applying saturation to it.

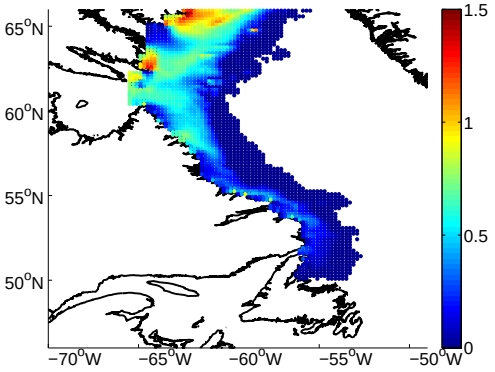

(a) Background State x^b

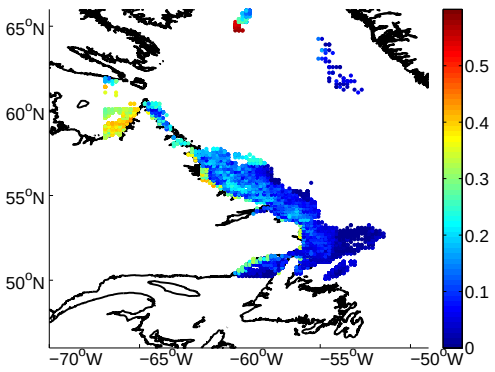

(b) MODIS observations

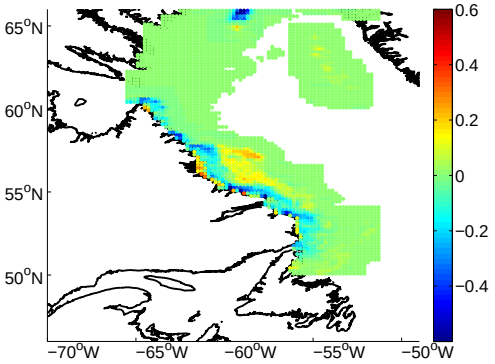

(c) Analysis increment without saturation for MODIS

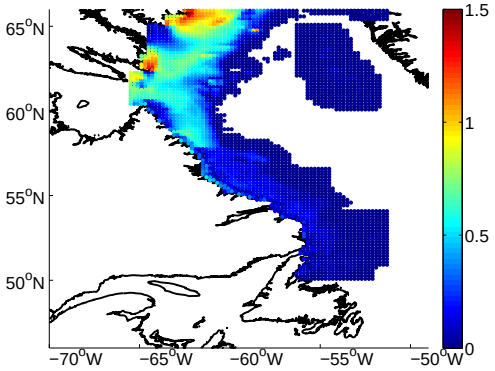

(d) Analysis without saturation for MODIS observations

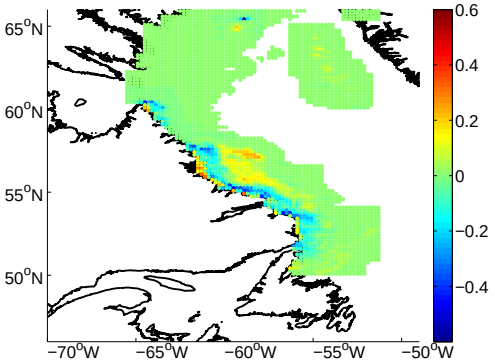

(e) Analysis increment with saturation for MODIS

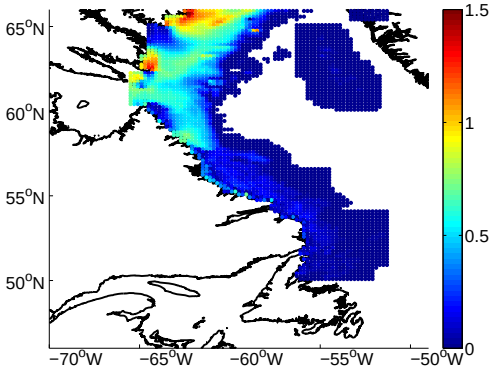

(f) Analysis with saturation for MODIS observations

Figure 5.8: MODIS analysis results with and without saturation where panel (f) analysis is obtained by applying 0.5 m saturation to H operator. Not much difference is seen between panels (d) and (f) as all observations for January 24 2007 has ice thickness value less than 0.5 m

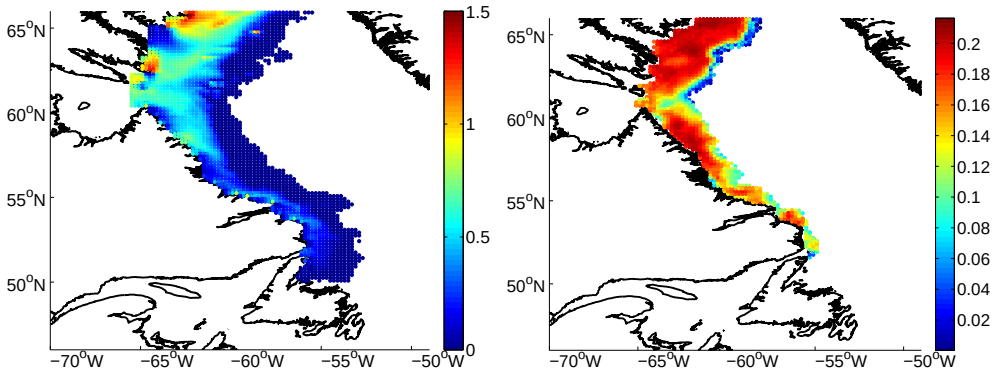

(a) Background State x^b (b) AMSR-E observations

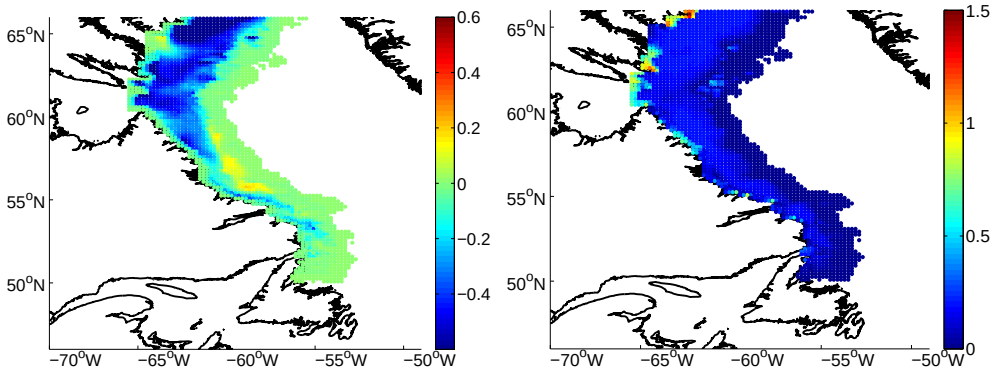

(c) Analysis Increment without saturation for AMSR-E (d) Analysis without saturation for AMSR-E observations

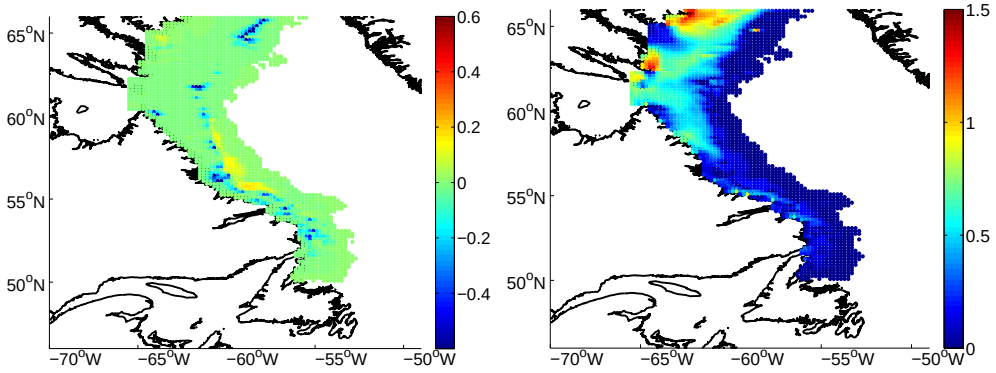

(e) Analysis Increment with saturation for AMSR-E (f) Analysis with saturation for AMSR-E observations

Figure 5.9: AMSR-E analysis results with and without saturation. Panels (c) and (d) shows analysis increment and analysis state greater than 0.2 m , which is not correct. Panels (e) and (f) shows analysis increment and analysis state with linear forward model applied to ice thickness value less than 0.2 m and saturation function to that more than 0.2 m.

Sea ice thickness estimates with saturation of 0.2 m are shown in Figure 5.9f. When compared with figure 5.3e, it shows how saturation affected the estimates for $H(\mathbf{x}^b)$. It can be seen that all values above 0.2 m (red pixel) are masked while those below 0.2 m are not affected. From figure 5.9f, it is clear that the AMSR-E estimates are closer to observations.

Table 5.2: Means and standard deviation and mean for difference between estimated ice thickness and CIS ice data for January 24, 2007 demonstrating the impact of saturation on estimation

Experiment	Observation error Standard deviation	Mean Analysis - Ice Charts (m)	Standard deviation Analysis - Ice Charts (m)	Mean Background - Ice Charts (m)	Standard deviation Background - Ice Charts (m)
Case 1 with MODIS (without saturation)	0.15	0.0099	0.0728	0.0084	0.0727
Case 2 with MODIS (with saturation)	0.15	0.0099	0.0728	0.0084	0.0727
Case 3 with AMSR-E (without saturation)	0.03	0.0205	0.0614	0.0084	0.0727
Case 4 with AMSR-E (with saturation)	0.03	0.0001	0.0830	0.0084	0.0727

Results shown in figure 5.8 and 5.9 were required to be verified. It was done by evalu-

ating the estimates of sea ice thickness in terms of standard deviation of differences with daily CIS ice charts as shown in table 5.2. The second column of the table represents observation error standard deviation. It can be observed that for AMSR-E, the mean of the difference between estimated ice thickness and that from CIS daily ice charts is much less than for the experiment with saturation (0.0011) when compared to one without saturation (0.0205), but there is not much difference in their standard deviation values. While for MODIS, mean of the difference between estimated ice thickness and that from CIS daily ice charts is 0.0099 and standard deviation is 0.0728 for both the cases. It can be concluded that values with saturation are much closer to charts than the one without saturation for AMSR-E while saturation has no effect on MODIS analysis as MODIS observations for the day had ice thickness values less than threshold.

5.2.3 Estimation for January 2007

There is substantial variation in ice cover over the east coast of Canada in the month of January due to both winds and temperature changes. The ice edge expands seawards and spreads southward. In the northern part of the domain the ice cover is closely packed for a distance from the coast to the sea. New ice starts accumulating in the beginning of January as grey or grey-white ice towards the southern Labrador coast. By the end of the month, ice cover from the coast becomes loose and starts drifting toward the south-east [16].

Ice thickness was estimated over the Labrador coast for the month of January 2007 using data fusion technique. The observations consisted of remote sensing data from AMSR-E that is combined with the background state using optimal interpolation to produce estimates of the ice thickness state. These estimates were then compared with ice thickness

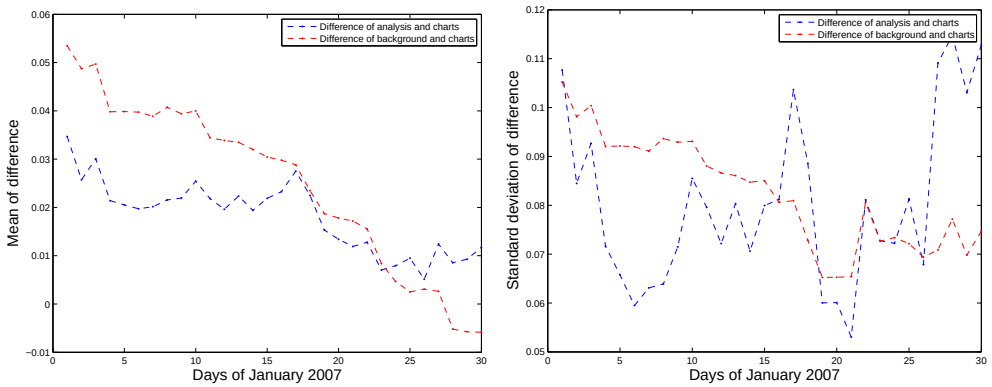

(a) Mean of difference of Analysis and Ice Charts for AMSR-E with $\sigma_o = 0.2$

(b) Standard Deviation of difference of Analysis and Ice Charts for AMSR-E with $\sigma_o = 0.2$

Figure 5.10: Mean and standard deviation for the difference of analysis and ice charts for the month of January 2007 with $\sigma_o = 0.2$ when observations from AMSR-E are used

information obtained from daily ice charts.

Figure 5.10 shows the mean and the standard deviation for the difference between the analysis with $\sigma_o = 0.2$ for AMSR-E observations and ice thickness derived from ice charts for the month of January 2007. The red line represents the difference between background state and charts while the blue line represents the difference between analysis state and charts. It may be observed that mean and standard deviation of the difference vary largely from January 1 to 16, i.e. the difference from analysis state is much lower than from the background state. Thus, it may be concluded that the results from the analysis are closer to the ice charts thickness values. There is not much difference between results from the analysis and background from January 17 to 26. Some difference in the results is observed on proceeding towards the end of January. This may be due to the lower number of observations from 1 to 16 and 27 to 30 January. The $\sigma_o = 0.2$ did not had much effect

on analysis from 17 to 26 January thus causing analysis to be near to background.

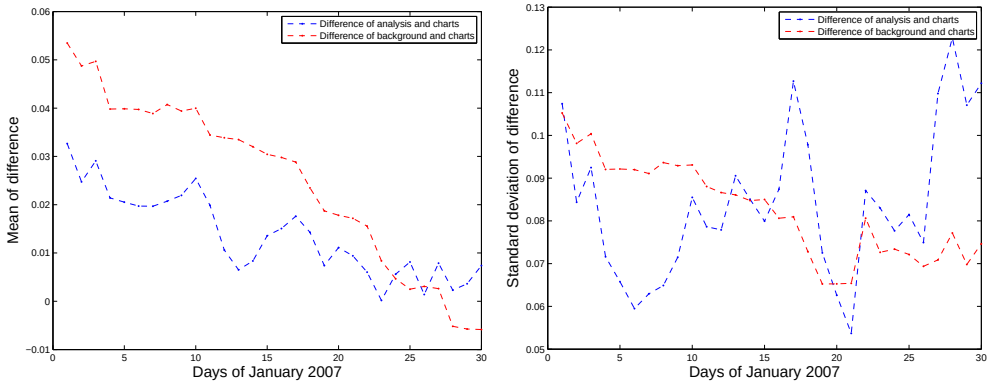

(a) Mean of difference of Analysis and Ice Charts for AMSR-E with $\sigma_o = 0.03$

(b) Standard Deviation of difference of Analysis and Ice Charts for AMSR-E with $\sigma_o = 0.03$

Figure 5.11: Mean and standard deviation for the difference of analysis and ice charts for the month of January 2007 with $\sigma_o = 0.03$ when AMSR-E observations are used

Figure 5.11 shows the mean and the standard deviation for the difference between the analysis with $\sigma_o = 0.03$ with AMSR-E observations and ice thickness derived from ice charts for the month of January 2007. It can be observed that mean of the difference vary largely from January 1 to 23 i.e. the difference from analysis state is much lower than that from the background state while the standard deviation does not show such a pattern. The mean then increases for the difference of analysis and charts in comparison to that from background and charts indicating poor results. But, when evaluating results over the entire time period of the study estimates with $\sigma_o = 0.03$ are better than those with $\sigma_o = 0.2$, with analysis being closer to charts.

5.3 Application in ship routing

This section is about a potential application of our research work. In this section an improved route for a ship is found through ice-infested water. Data fusion is used to improve the ship's route by combining a state estimate with observations of ice thickness. The Dijkstra algorithm [80] is used to find the path from a specified source to a specified destination. Initially it is assumed to be a toy problem that could be expanded in the future to cover a more realistic domain.

5.3.1 Motivation

In the last few years, there has been a great increase in energy consumption and the price of oil. To compensate this increased demand, new sources of energy and oil resources are being investigated. The Arctic region has the potential to fulfil these increasing demands. But to access natural resources in the Arctic region, ship routes need to be developed. At the same time, there has been accelerated Arctic ice melting, resulting in improved access to this area. The NSR along Russia and the NWP through the Canadian Arctic archipelago were finally open in 1991 and 2009 respectively, allowing navigation between the Pacific and the Atlantic oceans through the Arctic [57].

Geometrically, the NSR or NWP routes are shorter routes compared to the conventional routes that pass through the Suez and the Panama Canal. This shorter path noticeably saves time and expense. But navigating the NSR or NWP is difficult due to the harsh environmental conditions. The resulting technical difficulties make it challenging for year-round commercial shipping [57].

The problem of a ship becoming stuck in thick ice can be resolved if ice thickness and

ice pressure values are known for the area through which a ship has to traverse. Simulating navigational routes in an Arctic region is beneficial to shipping companies and for search and rescue operations. These routes help them dispatch ice-breakers in the right path for maximum ice breaking without becoming stuck in the thick ice cover. It can also help icebreakers to hit the right spot and avoid making excessive icebergs [57].

5.3.2 Method for path finding

One of the traditional methods to find the path between two points in a given domain is the Dijkstra method. The Dijkstra algorithm was invented by computer scientist Edsger Dijkstra in 1956 and was published in 1959 [80]. It is a graph search algorithm that finds the shortest path from a source to a target. This is done by assigning a weight to each node and then connecting nodes with minimum distance between them. It is based on two assumptions i.e. there is only one single source and the weight given to a node must be positive.

Figure 5.12a is a grey-scale image of the area under study. This image is taken from a satellite borne synthetic aperture radar sensor, and is relatively high resolution ($\approx$ 100 pixel spacing). The first step is to discretize the area of study and convert it from grey scale to an image containing representative ice thickness values at each point. The value at each point is then normalized to represent ice thickness; this is referred to as the true ice thickness.

A low pass Gaussian filter is applied to the true ice thickness to mimic the spatial averaging that occurs when the true state is imaged by a passive microwave or VIS/IR sensor. This is referred to as the true background state ice thickness.

The true background state ice thickness is perturbed with Gaussian random noise of

0.2 standard deviation to obtain the background state ice thickness. Figure 5.12b shows the true ice thickness and figure 5.12c shows the background ice thickness calculated by applying Gaussian smoothing with a scale of 10 units to true ice thickness state.

To find the path through this region a function, ψ, with the ice thickness at each point in the region of study is defined. The ψ function can be the true state, true background state or background state based on the ice thickness estimates required to compute optimal path for ships.

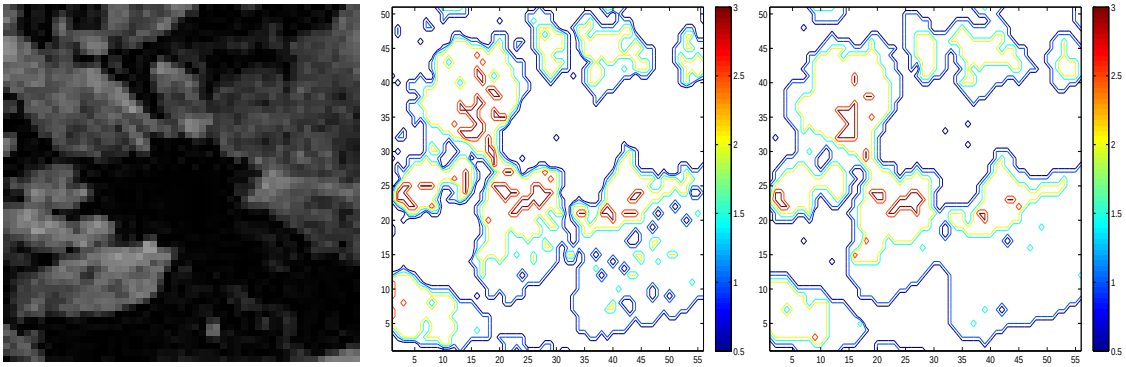

(a) Grey-scale image (b) Dijkstra graph of the true ice thickness (c) Dijkstra graph of the background ice thickness

Figure 5.12: Grey scale image with its true and background ice thickness. Panel (a) is an image taken from a SAR sensor over Baffin bay and is rescaled to obtain values representative of ice thickness, referred to as the true ice thickness shown in panel (b). Panel (c) represents background ice thickness obtained by applying low pass Gaussian filter to (b).

The node at which a ship will start is called the source node and the destination node is called the target node. There is a set called visited and a set called unvisited, which keeps track of the nodes visited and unvisited respectively. Those are required to track the

final optimal route computed using the Dijkstra algorithm.

The various steps involved in computing the path from the source node to the target node are explained below.

1. Assign weights to all the nodes. Set the weight for all nodes to infinity and that of current node to zero.

2. Mark all nodes as unvisited. Set the source node as the current node.

3. For a small domain surrounding the current node, find the total weights for each node. This weight is the sum of the weight of the current node, the normalized ice thickness at its neighbouring node and the normalized distance of the neighbour node from the current node. The weight function is described by equation 5.16 which assumes that weight at various points is given by a matrix **w** and point (a,b) represents the current node while (a+i,b+j) is its neighbouring node. $\boldsymbol{\psi}$ represents a matrix with ice thickness values for all nodes defined in the domain. Weight function can be mathematically represented as w(a,b).

$$w(a+i, b+j) = w(a, b) + \psi(a+i, b+j) + (i^2 + j^2)^{1/2} \tag{5.16}$$

4. When weights for all neighbours are calculated then the node with the smallest weight in the unvisited set becomes our new current node.

5. Mark the current node as visited and remove it from the unvisited set.

6. If the destination node is marked as visited then stop else all steps from step 3 are repeated until the destination is reached.

5.3.3 Results for Ship Routing

The input for the experiments is the test image shown in figure 5.12a. This test image is used to compute the true state, the background state and the true background state of ice thickness.

To simulate a practical application in which way-points may be used for navigation, the image is divided into two sub-images. Splitting the image into two sub-images also accelerated the computation of the analysis state. The Dijkstra algorithm is applied to each sub-image to calculate the path from the source to the target node. After the paths are computed separately for two sub-images are combined to appear as one image. Figure 5.13 shows the paths calculated for the true ice thickness, the background ice thickness and the analysis, that is when the observations are fused into each sub-image.

In this experiment, three assumptions are made for assimilating the background state and perturbed observations. The first is that observation error covariance matrix, $\mathbf{R}$, is assumed to be a diagonal matrix with standard deviation of 0.2. The second is that no saturation is applied on the observation operator, H. Lastly, the background error covariance matrix, $\mathbf{B}$, is assumed to have a length scale of 2 units. BLUE is used to produce the analysis state.

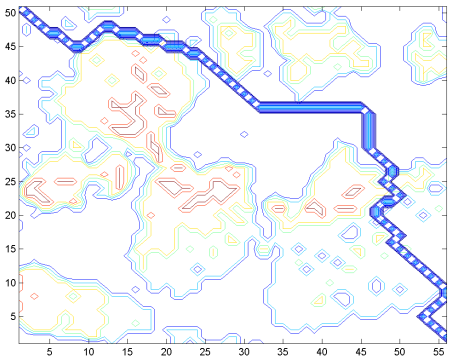

(a) path from true ice thickness on true state

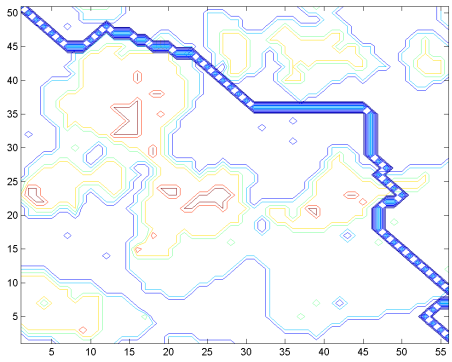

(b) path from background ice thickness on background state

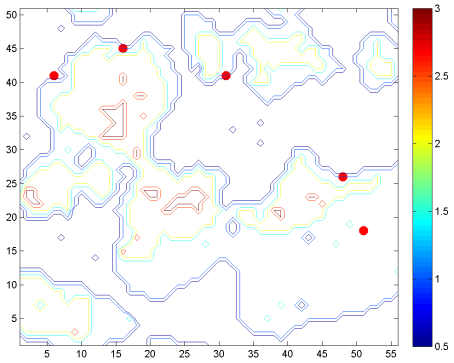

(c) background ice thickness with observations

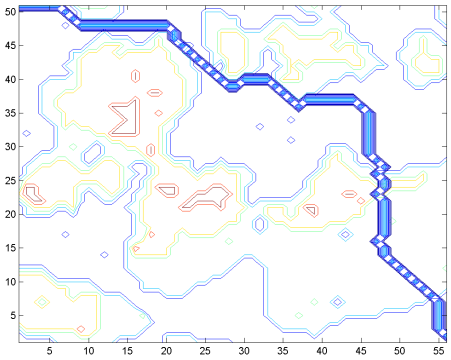

(d) path from data fusion using ice thickness with $\sigma_o = \sigma_b$ on background state

Figure 5.13: Path calculated using Dijkstra algorithm on true, background and analysis ice thickness where colored contour levels represent the ice thickness. Total thickness of ice covered is observed to be less with data fusion as shown in panel (d) in comparison to that in true ice thickness, panel (a), and background ice thickness, panel (b).

Table 5.3 shows result for different cases for which the total ice thickness traversed

and distance travelled is calculated. Total thickness of ice traversed by ship is calculated as the sum of the true ice thickness values at the points through which ship traversed. Total distance covered is the sum of the distance between two consecutive points traversed by ship. For the true state and the background state, the path is directly calculated by applying Dijkstra algorithm on the aforementioned states and the results are shown in figure 5.13a and 5.13b respectively.

Results from experiments with different values of σ_o are also shown in table 5.3. The data fusion experiments were carried out using three different values of the ratio of background error standard deviation to observation error standard deviation, $\gamma = \sigma_o^2/\sigma_b^2$. As the value of γ decreases, the observation will have increased weight accordingly in the analysis. The standard deviation of noise used to perturb the background (σ_b) was 0.2 while that used to perturb observations varied between σ_b to $\sigma_b/4$. Figure 5.13d shows the path through assimilated state for observations in figure 5.13c with standard deviation $\sigma_o = \sigma_b$ for Gaussian smoothing of 10 units.

It is also shown that when the ship has knowledge of the background state or true state, the thickness of ice traversed is greater. This would result in a more expensive operation for the ship in terms of fuel consumed. The path length increases and thickness of ice traversed decreases when observations are assimilated. The length of the path is seen to increase as the observation error standard deviation is decreased.

Table 5.3: Total thickness of ice traversed and distance covered for various values of σ_o used in data fusion as compared to the aforementioned values with true state and background state.

Cases	total thickness of ice traversed	total distance covered
true state	28	4056.2
background state	24	4108.5
fusion $\sigma_o = \sigma_b$	23	4129.5
fusion $\sigma_o = \sigma_b/2$	23	4130.4
fusion $\sigma_o = \sigma_b/4$	23	4131.5

In figure 5.14 two different sets of observation are used to assimilate a ship route. Figure 5.14a and 5.14c shows these observations as red dots on true ice thickness state. These observations are perturbed with a standard deviation same as that of the background error. Figure 5.14b and 5.14d shows different paths calculated for different sets of observations assimilated with background state.

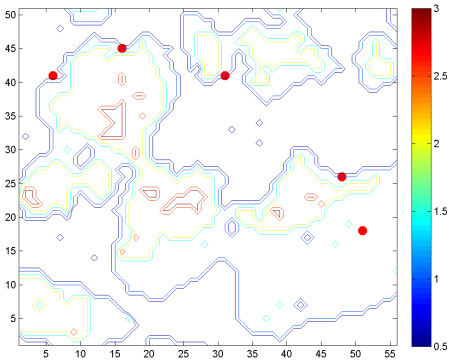

(a) true ice thickness with observations shown as red dots

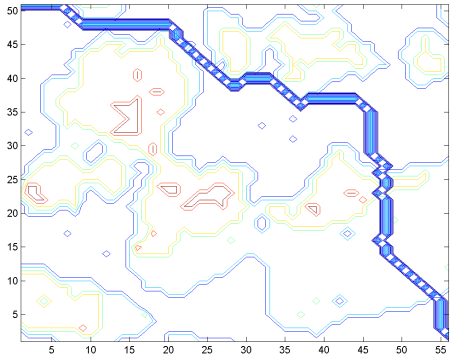

(b) path from assimilated ice thickness with observations shown in (a)

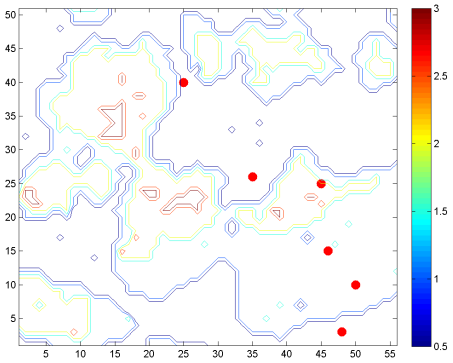

(c) true ice thickness with observations shown as red dots

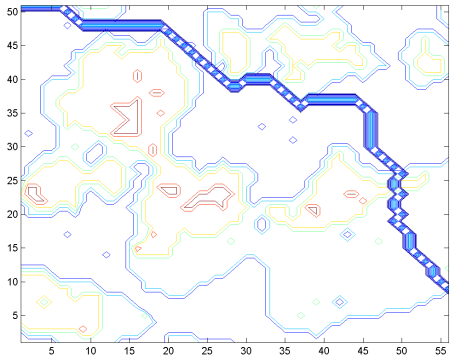

(d) path from assimilated ice thickness with observations shown in (c)

Figure 5.14: Path calculated in panels (b) and (d) uses Dijkstra algorithm for different sets of observations ,shown as red dots in panels (a) and (c), with $\sigma_o = \sigma_b$

5.4 Summary

In this chapter, various parameters for data fusion technique are calculated. The spatial correlation in the background error covariance matrix (**B**) is calculated by a normalized diffusion operator. This diffusion operator is calculated by using an explicit method with the Dirchilet boundary condition at sea coast and the Neumann boundary condition at open sea coast. The observation operator (H) is calculated by applying linear forward model to all ice thickness values of background state below threshold and saturation to ice thickness value of background state more than threshold. The observation error covariance matrix, **R**, is assumed to be diagonal with observation error standard deviation, σ_o, 0.03 for AMSR-E observations. This chapter also applied data fusion technique to improve ship path by using estimated ice thickness values to find navigation route through ice covered water. The total distance covered increased and the total ice thickness traversed decreased for assimilated ice thickness estimates when compared to the true ice state and the background ice state estimates. The next chapter presents conclusion on the research work presented in this thesis.

Chapter 6

Conclusion

In this thesis, data fusion has been used to estimate ice thickness based on an optimal interpolation technique. The method combines ice thickness values from models and observations to produce better estimates of ice thickness states. The sea ice thickness from a model and observations from AMSR-E and MODIS are used for the month of January, 2007. Daily ice charts from CIS are used to verify the estimated ice thickness.

AMSR-E and MODIS sensors have a limitation that they cannot measure ice thickness of more than 0.2 m and 0.5 m respectively. Hence, observation operator (H) was limited by saturating all values above the threshold of 0.2 m for AMSR-E and 0.5 m for MODIS, while applying linear forward model to all values below the threshold. AMSR-E, with saturation, produced results closer to that from the ice charts while saturation had no effect of MODIS, as MODIS observations were less than applied threshold. Difficulties were encountered in using the non-linear H operator in that it was difficult for the analysis to reach convergence. In the future an alternative H operator or different approach should be investigated.

The background error covariance matrix ($\mathbf{B}$) is calculated by solving the diffusion equation with the length scale of 2 units. Also, Dirtchlet and Neumann boundary conditions were applied to evaluate diffusion operator at the coast and at the boundary with sea.

Using a lower value of observation error standard deviation (σ_o) increased the impact of ice thickness observations and brought analysis closer to the ice thickness from the ice charts. It was observed that AMSR-E produced good results with $\sigma_o = 0.03$ and MODIS with $\sigma_o = 0.2$.

Later AMSR-E ice thickness values were fused with model states for the month of January 2007 with $\sigma_o = 0.2$ and $\sigma_o = 0.03$. It was observed that data fusion produced good results with $\sigma_o = 0.03$, for AMSR-E, from 17 to 26 January, 2007. This improvement in results from 17 to 26 January was due to the higher number of observations that contributed in greater impact on the data fusion for this period.

The method discussed in this thesis can be used to find improved paths for ships, which is illustrated with a toy example. The input to the method is a grey-scale image which is then used to compute the true state and the background state while the BLUE algorithm is used to find the analysis ice thickness state. Here, it is assumed $\mathbf{R}$ is diagonal, $\mathbf{B}$ is computed with diffusion length scale of 2 units and no saturation is needed for the H operator. The Dijkstra algorithm is used to find the optimal path for ships through ice-infested sea. Total ice thickness traversed was less and total distance covered by a ship was more in the toy example when data fusion was used in comparison to the true and the background state. It also depends on the ratio between observation and background error standard deviation. Better results are obtained when standard deviation for observation is same as that for the background, $\sigma_o = \sigma_b$.

6.1 Future work

The research work can be further expanded by using

- the data assimilation technique to combine the model state and the observations to provide estimates that are fed back to a prognostic ice ocean model.
- Different saturation function to calculate observation operator, H, for AMSR-E and MODIS can be further investigated.

6.2 Summary

The thesis uses data fusion technique to combine ice thickness observations from model and observations from AMSR-E and MODIS to produce state estimates that are near to CIS chart analysis. In the data fusion method, the spatial correlation in **B** is calculated using a diffusion operator, H is applied with saturation and **R** is a diagonal matrix. Results obtained look feasible for AMSR-E. MODIS did not show good results due to cloud cover for most of the days of January 2007. This study is combined with a path calculation algorithm to improve ship navigation through thick ice.

Appendix A

Deriving relation between weighting factor (W) and Kalman gain (K)

In this section, relation between weighting factor and Kalman gain is derived. For this equation A.1 is taken from section 4.2

$$\mathbf{x}^t + \mathbf{e}^a = \mathbf{W}(\mathbf{x}^t + \mathbf{e}^b) + \mathbf{K}(\mathbf{H}(\mathbf{x}^t) + \mathbf{e}^o) \tag{A.1}$$

On applying the expectation operator on equation A.1 gives

$$< \mathbf{x}^t > + < \mathbf{e}^a >= \mathbf{W} < \mathbf{x}^t > + \mathbf{W} < \mathbf{e}^b > + \mathbf{KH} < \mathbf{x}^t > + \mathbf{K} < \mathbf{e}^o > \tag{A.2}$$

It is assumed that errors are unbiased with $<\mathbf{e}^{\mathrm{o}}>$, $<\mathbf{e}^{\mathrm{b}}>$, $<\mathbf{e}^{\mathrm{a}}>= 0$

$$< \mathbf{x}^t > + 0 = \mathbf{W} < \mathbf{x}^t > + \mathbf{W} * 0 + \mathbf{KH} < \mathbf{x}^t > + \mathbf{K} * 0 \tag{A.3}$$

$$< \mathbf{x}^t >= (\mathbf{W} + \mathbf{KH}) < \mathbf{x}^t > \tag{A.4}$$

Cancelling $< \mathbf{x^t} >$ on both sides

$$\mathbf{I} = \mathbf{W} + \mathbf{KH} \tag{A.5}$$

or

$$\mathbf{W} = \mathbf{I} - \mathbf{KH} \tag{A.6}$$

Appendix B

Calculating normalized background error covariance matrix (B) from diffusion operator (q)

Background error covariance matrix ($\mathbf{B}$) is calculated as the product of the diagonal matrix of background error standard deviation ($\mathbf{D}$), correlation matrix ($\mathbf{C}$) and $\mathbf{D}$ again, as can be seen in equation B.1.

$$\mathbf{B} = \mathbf{DCD} = \mathbf{DC}^{1/2}(\mathbf{DC}^{1/2})^T \tag{B.1}$$

$\mathbf{C}$ matrix is decomposed into horizontal ($\mathbf{C}_h$) and vertical ($\mathbf{C}_v$) correlation matrices as shown in equation B.2.

$$\mathbf{C} = \mathbf{C}_v\mathbf{C}_h \tag{B.2}$$

It is assumed that vertical correlation matrix is identity matrix and the square root of the horizontal correlation matrix is given as product of $\mathbf{a}$ and square root of $\mathbf{q}$ as seen in equation B.3, where $\mathbf{a}$ is the normalization factor and $\mathbf{q}$ is the diffusion operator calculated

by solving diffusion equation [66].

$$\mathbf{C}_h^{1/2} = \mathbf{a}\mathbf{q}^{1/2} \tag{B.3}$$

where

$$\mathbf{a} = \left(diag\left\{ \frac{1}{K-1} \sum_{k=1}^{K+1} \widehat{\mathbf{v}_k}\widehat{\mathbf{v}_k}^T \right\} \right)^{-1/2} \tag{B.4}$$

and

$$\widehat{\mathbf{v}_k} = \mathbf{q}^{1/2}\mathbf{v}_i \tag{B.5}$$

Here $\mathbf{v}_k$ represents independently and normally distributed random numbers with $E[\mathbf{v}_k] = 0$ and $E[\mathbf{v}_k\mathbf{v}_k^T] = I$. K is the number of samples over which $\mathbf{v}_k$ is distributed [66].

References

[1] Meteorological Service of Canada (2005). *Manual of Standard Procedures for Observing and Reporting Ice Conditions (MANICE)*. Ninth Edition, Crown, Canadian Ice Servive, Environment Canada, Ottawa, 146pp.

[2] K.A. Scott, M. Buehner and T. Carrieres (2014). An assessment of sea-ice thickness along the Labrador Coast from AMSR-E and MODIS data for operational data assimilation. *Geoscience and Remote Sensing, IEEE Transactions*, 52(5):2726–2737.

[3] J. Hagelaars. Melting of the arctic sea ice (2012). My view on Climate change. <https://ourchangingclimate.wordpress.com/2013/03/25/melting-of-the-arctic-sea-ice >.

[4] Y. Yu, G.A. Maykut and D.A. Rothrock (2004). Changes in the thickness distribution of Arctic sea ice between 1958–1970 and 1993–1997. *Journal of Geophysical Research: Oceans*, 109(C8):doi:10.1029/2003JC001982.

[5] R. Gran and M.J. Viñas. NASA finds thickest parts of arctic ice cap melting faster (2012). <http://www.nasa.gov/topics/earth/features/thick-melt.html >.

[6] R. Faragher (2012). Understanding the basis of the kalman filter via a simple and intuitive derivation [lecture notes]. *Signal Processing Magazine, IEEE*, 29(5):128–132.

[7] M. Johnson, A. Proshutinsky, Y. Aksenov, A.T. Nguyen, R. Lindsay, C. Haas, J. Zhang, N. Diansky, R. Kwok, W. Maslowski, S. Hkkinen, I. Ashik and B. Cuevas (2012). Evaluation of Arctic sea ice thickness simulated by Arctic Ocean Model Intercomparison Project models. *Journal of Geophysical Research: Oceans*, 117(C8):doi:10.1029/2011JC007257.

[8] A. Schweiger, R. Lindsay, J. Zhang, M. Steele, H. Stern and R. Kwok (2011). Uncertainty in modeled Arctic sea ice volume. *Journal of Geophysical Research: Oceans*, 116(C8):doi:10.1029/2011JC007084.

[9] S. Nihashi, K.I. Ohshima, T. Tamura, Y. Fukamachi and S.I. Saitoh (2009). Thickness and production of sea ice in the Okhotsk Sea coastal polynyas from AMSR-E. *Journal of Geophysical Research: Oceans*, 114(C10):10.1029/2008JC005222.

[10] K. Naoki, J. Ukita, F. Nishio, M. Nakayama, J.C. Comiso and A. Gasiewski (2008). Thin sea ice thickness as inferred from passive microwave and in situ observations. *Journal of Geophysical Research: Oceans*, 113(C2):doi:10.1029/2007JC004270.

[11] Y. Yu and R.W. Lindsay (2003). Comparison of thin ice thickness distributions derived from RADARSAT Geophysical Processor System and advanced very high resolution radiometer data sets. *Journal of Geophysical Research: Oceans*, 108(C12):doi: 10.1029/2002JC001319.

[12] X. Wang, J.R. Key and Y. Liu (2010). A thermodynamic model for estimating sea and lake ice thickness with optical satellite data. *Journal of Geophysical Research: Oceans*, 115(C12):doi:10.1029/2009JC005857.

[13] S. Polavarapu (2012). Introduction - Earth, Atmospheric, and Planetary Physics

Chapter-1 Data Assimilation. University of Toronto. <http://www.atmosp.physics.utoronto.ca/PHY2509/ch1.pdf >.

[14] X. Zou, F. Vandenberghe, B. Wang, M.E. Gorbunov, Y.H. Kuo, S. Sokolovskiy, J.C. Chang, J.G. Sela and R.A. Anthes (1999). A ray-tracing operator and its adjoint for the use of GPS/MET refraction angle measurements. *Journal of Geophysical Research: Atmospheres*, 104(D18):22301–22318.

[15] J.C. Comiso and F. Nishio (2008). Trends in the sea ice cover using enhanced and compatible AMSR-E, SSM/I, and SMMR data. *Journal of Geophysical Research: Oceans*, 113(C2):doi: 10.1029/2007JC004257.

[16] Environment Canada (2013). Ice along the East Coast - too thin and too thick. <http://www.ec.gc.ca/meteo-weather/default.asp?lang=En&n=1BF890AC-1#s5>.

[17] D.A. Rothrock, Y. Yu and G.A. Maykut (1999). Thinning of the Arctic sea-ice cover. *Geophysical Research Letters*, 26(23):3469–3472.

[18] J. Liu, M. Song, R.M. Horton and Y. Hu (2013). Reducing spread in climate model projections of a September ice-free Arctic. *Proceedings of the National Academy of Sciences*, 110(31):12571–12576.

[19] H. Eicken (2013). Ocean science: Arctic sea ice needs better forecasts. *Nature*, 497(7450):431–433.

[20] Q. Yang, S.N. Loza, M. Losch, J. Liu, Z. Zhang, L. Nerger and H. Yang (2015). Assimilating summer sea-ice concentration into a coupled ice ocean model using a LSEIK filter. *Annals of Glaciology*, 56(69):38–44.

[21] M. Ghil (1989). Meteorological data assimilation for oceanographers. Part I: Description and theoretical framework. *Dynamics of Atmospheres and Oceans*, 13(3):171–218.

[22] R.A. Panofsky (1949). Objective weather map analysis. *Journal of the Atmospheric Sciences*, 6(6):386–392.

[23] J.G. Charney, R. Fjörtoft, and J.v. Neumann (1950). Numerical integration of the barotropic vorticity equation. *Tellus*, 2(4):237–254.

[24] M. Ghil and P. Malanotte-Rizzoli (1991). Data assimilation in meteorology and oceanography. *Advances in geophysics*, 33:141–266.

[25] A. Eliassen (1954). *Provisional Report on calculation of Spatial Covariance and Autocorrelation of the Pressure field*. Institute of Weather and Climate Research,Academy of Science Oslo, Report no. 5:12pp.

[26] L.S. Gandin (1966). Objective analysis of meteorological fields. *Quarterly Journal of the Royal Meteorological Society*, 92(393):447–447.

[27] N.A. Phillips (1976). Impact of synoptic observing and analysis systems on flow pattern forecasts. *Bulletin of the American Meteorological Society*, 57:1225–1250.

[28] G. P. Cressman (1959). An operational objective analysis system. *Monthly Weather Review*, 87(10):367–374.

[29] B. Gilchrist and G.P. Cressman (1954). An experiment in objective analysis. *Tellus*, 6(4):309–318.

[30] L. Bengtsson and J. Shukla (1988). Integration of space and in situ observations to study global climate change. *Bulletin of the American Meteorological Society*, 69(10):1130–1143.

[31] C. Jamet and H. Loisel (2013). Data Assimilation Methods in. *Surface OceanLower Atmosphere Processes*. American Geophysical Union, Washington D. C., 303–317.

[32] A. Gelb (1974). *Applied Optimal Estimation*. MIT press, Cambridge MA, 382pp.

[33] J.L. Lions (1971). *Optimal Control of Systems Governed by Partial Differential Equations*. First Edition, Springer, Verlag Berlin Heidelberg, 400pp.

[34] S.E. Cohn (1997). An introduction to estimation theory. *Journal-Meteorological Society of Japan Series*, 2(75):147–178.

[35] A.C. Lorenc (1981). A global three-dimensional multivariate statistical interpolation scheme. *Monthly Weather Review*, 109(4):701–721.

[36] P.J. Van Leeuwen and G. Evensen (1996). Data assimilation and inverse methods in terms of a probabilistic formulation. *Monthly Weather Review*, 124(12):2898–2913.

[37] P. Courtier (1997). Variational methods. *Journal-Meteorological Society of Japan Series*, 75:211–218.

[38] R.E. Kalman (1960). A new approach to linear filtering and prediction problems. *Journal of Fluids Engineering*, 82(1):35–45.

[39] P.L. Houtekamer and H.L. Mitchell (1998). Data assimilation using an ensemble Kalman filter technique. *Monthly Weather Review*, 126(3):796–811.

[40] K. Ide and M. Ghil (1998). Extended Kalman filtering for vortex systems. Part I: Methodology and point vortices. *Dynamics of Atmospheres and Oceans*, 27(1):301–332.

[41] K. Ide and M. Ghil (1998). Extended Kalman filtering for vortex systems. Part II: Rankine vortices and observing-system design. *Dynamics of Atmospheres and Oceans*, 27(1):333–350.

[42] D.R. Thomas and D.A. Rothrock (1989). Blending sequential scanning multichannel microwave radiometer and buoy data into a sea ice model. *Journal of Geophysical Research: Oceans*, 94(C8):10907–10920.

[43] D.R. Thomas and D.A. Rothrock (1993). The Arctic Ocean ice balance: A Kalman smoother estimate. *Journal of Geophysical Research: Oceans*, 98(C6):10053–10067.

[44] D. Thomas, S. Martin, D. Rothroc and M. Steele (1996). Assimilating satellite concentration data into an Arctic sea ice mass balance model, 1979-1985. *Journal of Geophysical Research: Oceans*, 101(C9):20849–20868.

[45] K.A. Lisaeter, J. Rosanova and G. Evensen (2003). Assimilation of ice concentration in a coupled ice-ocean model, using the Ensemble Kalman filter. *Ocean Dynamics*, 53(4):368–388.

[46] J.L. Lieser (2004). *A numerical model for short-term sea ice forecasting in the Arctic*. PhD thesis, Universitaet Bremen, Germany, 105pp.

[47] W.N. Meier, J.A. Maslanik and C.W. Fowler (2000). Error analysis and assimilation of remotely sensed ice motion within an Arctic sea ice model. *Journal of Geophysical Research: Oceans*, 105(C2):3339–3356.

[48] T. Arbetter, A. Lynch, J. Maslanik and W. Meier (2002). Effects of data assimilation of ice motion in a basin-scale sea ice model. Ice in the Environment:Proceedings of the 16th IAHR International Symposium on Ice, Dunedin, New Zealand, 8pp.

[49] W.N. Meier and J.A. Maslanik (2003). Effect of environmental conditions on observed, modeled, and assimilated sea ice motion errors. *Journal of Geophysical Research: Oceans*, 108(C5):doi: 10.1029/2002JC001333.

[50] J. Zhang, D.R. Thomas, D.A. Rothrock, R.W. Lindsay, Y. Yu and R. Kwok (2003). Assimilation of ice motion observations and comparisons with submarine ice thickness data. *Journal of Geophysical Research: Oceans*, 108(C6):doi: 10.1029/2001JC001041.

[51] R.W. Lindsay, J. Zhang and D.A. Rothrock (2003). Sea-ice deformation rates from satellite measurements and in a model. *Atmosphere-Ocean*, 41(1):35–47.

[52] R. W. Lindsay and J. Zhang (2006). Assimilation of ice concentration in an ice–ocean model. *Journal of Atmospheric Oceanic Technology*, 23:742–749.

[53] V. Dulière and T. Fichefet (2007). On the assimilation of ice velocity and concentration data into large-scale sea ice models. *Ocean Science*, 3(2):321–335.

[54] J.D. Stark, J. Ridley, M. Martin and A. Hines (2008). Sea ice concentration and motion assimilation in a sea ice–ocean model. *Journal of Geophysical Research: Oceans*, 113(C5):doi: 10.1029/2007JC004224.

[55] K. Wang, J. Debernard, A.K. Sperrevik, P.E. Isachsen and T. Lavergne (2013). A combined optimal interpolation and nudging scheme to assimilate OSISAF sea-ice concentration into ROMS. *Annals of Glaciology*, 54(62):8–12.

[56] S. Tietsche, D. Notz, J. Jungclaus and J. Marotzke (2013). Assimilation of sea-ice concentration in a global climate model-physical and statistical aspects. *Ocean Science*, 9(1):19–36.

[57] J.H. Nam, I. Park, H.J. Lee, M.O. Kwon, K. Choi and Y.K. Seo (2013). Simulation of optimal arctic routes using a numerical sea ice model based on an ice-coupled ocean circulation method. *International Journal of Naval Architecture and Ocean Engineering*, 5:210–226.

[58] D. LaPrairie, M. Wilhelmson and K. Riska (1995). *A transit simulation model for ships in Baltic ice conditions : documentation of the calculation routine.* Helsinki University of Technology, Report M-200, 38pp.

[59] M. Patey and K. Riska (1999). *The NSR Simulation Study Work Package: Simulation of Ship Transit Through Ice.* INSROP Working Paper No. 155, Fridtjof Nansen Institute, Norway, 70pp.

[60] K. Kamesaki, S. Kishi and Y. Yamauchi (1999). *The NSR Simulation Study Work Package: Simulation of NSR Shipping Based on Year-round and Seasonal Operation Scenarios.* INSROP Working Paper No. 164, Fridtjof Nansen Institute, Norway, 136pp.

[61] N.D. Mulherin, D.T. Eppler, T.O. Proshutinsky, L.D. Farmer and O.P. Smith (1996). Development and results of a Northern Sea Route transit model. Technical report, No. CRREL-96-5. Cold Regions Research and Engineering Lab, Hanover, NH, 114pp.

[62] K.S. Choi, J.H. Nam, Y.J. Park, J.S. Ha and S.Y. Jeong (2010). Northern sea route transit analysis for large cargo vessels. In *The 25th International Symposium on Okhotsk Sea and Sea Ice.* 194-200.

[63] J.S. Ha, K.S. Choi, J.H. Nam and I.H. Park (2011). Supporting high latitude transit analysis with NSR NWP ice and environmental information. *The 26 th International Symposium on Okhotsk Sea and Sea Ice, Mombetsu, Japan.*

[64] T. Yao, C.L. Tang and I.K. Peterson (2000). Modeling the seasonal variation of sea ice in the Labrador sea with a coupled multicategory ice model and the Princeton ocean model. *Journal of Geophysical Research: Oceans*, 105(C1):1153–1165.

[65] J. Côté, S. Gravel, A. Méthot, A. Patoine, M. Roch and A. Staniforth (1998). The operational CMC-MRB global environmental multiscale (GEM) model. Part I: Design considerations and formulation. *Monthly Weather Review*, 126(6):1373–1395.

[66] A. Caya, M. Buehner and T. Carrieres (2010). Analysis and forecasting of sea ice conditions with three-dimensional variational data assimilation and a coupled ice-ocean model. *Journal of Atmospheric and Oceanic Technology*, 27:353–369.

[67] T. Tamura and K.I. Ohshima (2011). Mapping of sea ice production in the Arctic coastal polynyas. *Journal of Geophysical Research: Oceans*, 116(C7):doi:10.1029/2010JC006586.

[68] R.K. Singh, S.R. Oza, N.K. Vyas and A. Sarkar (2011). Estimation of thin ice thickness from the Advanced Microwave Scanning Radiometer-EOS for coastal polynyas in the Chukchi and Beaufort Seas. *Geoscience and Remote Sensing, IEEE Transactions*, 49(8):2993–2998.

[69] F. Wentz and T. Meissner (2000). *AMSRE Ocean Algorithm Theoretical Basis Document (Version 2)*. RSS Tech. Proposal 121599A-1, Remote Sensing Systems, Santa Rosa, CA, 74pp.

[70] D.K. Hall and G.A. Riggs (2007). Accuracy assessment of the MODIS snow-cover products. *HydrologicalProcesses*, 21(12):1534–1547.

[71] Y. Yu and D.A. Rothrock (1996). Thin ice thickness from satellite thermal imagery. *Journal of Geophysical Research: Oceans*, 101(C11):25753–25766.

[72] T. Carrieres, B. Greenan, S. Prinsenberg and I.K. Peterson (1996). Comparison of Canadian ice charts with surface observations off Newfoundland, winter 1992. *Atmosphere-Ocean*, 34(1):207–236.

[73] F. Bouttier and P. Courtier (2002). *Data Assimilation Concepts and Methods MARCH 1999*. Presented at the Meteorological Training Course Lecture Series. European Centre for Medium-Range Weather Forecasts, England, 58pp.

[74] M. Darvishi and G. Ahmadi (2014). Data assimilation techniques and modelling uncertainty in geosciences. *ISPRS-International Archives of the Photogrammetry, Remote Sensing and Spatial Information Sciences*, 1:85–90.

[75] M. Yaremchuk, M. Carrier, S. Smith and G. Jacobs (2013). *Background error correlation modeling with diffusion operators*. Springer Berlin Heidelberg, 177–203.

[76] D.N. Arnold (2011). *Lecture Notes on Numerical Analysis of Partial Differential Equations*. Prentice Hall, University of Minnesota, Minneapolis, United States, 88pp.

[77] A. Cheniguel (2014). Numerical method for the heat equation with Dirichlet and Neumann conditions. *Proceedings of the International MultiConference of Engineers and Computer Scientists*, I, IMECS, Hong Kong, 5pp.

[78] M.J. Carrie and H. Ngodock (2010). Background-error correlation model based on the implicit solution of a diffusion equation. *Ocean Modelling*, 35(12):45–53.

[79] TimeDomain CVD Inc. (2002). Fundamentals of chemical vapor deposition - diffusion length and dimensionless numbers. <http://www.timedomaincvd.com/CVD_Fundamentals/xprt/diffusion_length.html >.

[80] E.W. Dijkstra (1959). A note on two problems in connexion with graphs. *Numerische mathematik*, 1(1):269–271.

[81] K.A. Scott, M. Buehner, A. Caya and T. Carrieres (2012). Direct assimilation of AMSR-E brightness temperature for estimating sea ice concentration. *Monthly Weather Review*, 140:997–1013.

[82] N. Wiener (1956). Nonlinear prediction and dynamics. *Proceedings of the 3rd Berkeley Symposium on Mathematical Statistics and Probability*, 3:247–252, 1956.

[83] N. Wiener (1949). *Extrapolation, Interpolation, and Smoothing of Stationary Time Series*, volume 2. MIT Press, Cambridge MA, 176pp.